TITLE

Identifying developing interneurons as a potential target for multiple genetic autism risk factors in human and rodent forebrain.

AUTHORS/AFFILIATIONS

Yifei Yang[1,2], Sam A. Booker[1,2], James M. Clegg[1,2], Idoia Quintana Urzainqui[1,2], Anna Sumera[1,2], Zrinko Kozic[1,2], Owen Dando[1,2], Sandra Martin Lorenzo[3], Yann Herault[3], Peter C. Kind[1,2], David J. Price[1,2], Thomas Pratt[1,2,*]

[1]Simons Initiative for the Developing Brain,
[2]Centre for Discovery Brain Sciences,
Hugh Robson Building, Edinburgh Medical School Biomedical Sciences,
The University of Edinburgh, Edinburgh, EH8 9XD, United Kingdom.
[3]Université de Strasbourg, CNRS, INSERM, Institut de Génétique et de Biologie Moléculaire et Cellulaire, IGBMC, 1 rue Laurent Fries, 67404 Illkirch, France

CONTACT INFO

*Correspondence : t.pratt@ed.ac.uk

ABSTRACT

Autism spectrum condition or ‘autism’ is associated with numerous monogenic and polygenic genetic risk factors including the polygenic *16p11.2* microdeletion. A central question is what neural cells are affected. To systematically investigate we analysed single cell transcriptomes from gestational week (GW) 8-26 human foetal prefrontal cortex and identified a subset of interneurons (INs) first appearing at GW23 with enriched expression of a disproportionately large fraction of risk factor transcripts. This suggests the hypothesis that these INs are disproportionately vulnerable to mutations causing autism. We investigated this in a rat model of the *16p11.2* microdeletion. We found no change in the numbers or position of either excitatory or inhibitory neurons in the somatosensory cortex or CA1 of *16p11.2*$^{+/-}$ rats but found that CA1 Sst INs were hyperexcitable with an enlarged axon initial segment, which was not the case for CA1

pyramidal cells. This study prompts deeper investigation of IN development as a convergent target for autism genetic risk factors.

KEYWORDS

Development, telencephalon, autism, genetics, *16p11.2*, GABAergic, human, rat, electrophysiology, AIS.

Contributions and acknowledgements: YY and IQ performed bioinformatic analysis of human data, SAB, JMC, and AS performed rat experiments and analysis, ZK and OD contributed to linear modelling, SM and YH provided the *16p11.2* microdeletion rats, PCK and DJP contributed to design, TP designed the study and wrote the paper. This work was funded by the Simons Initiative for the Developing Brain (SFARI - 529085) and Biotechnology and Biological Sciences Research Council (BB/M00693X/1).

INTRODUCTION

Autism spectrum conditions (ASC – referred to here as 'autism') describe several symptoms and behaviours which affect the way in which a group of people understand and react to the world around them (Mental Health Foundation) and may co-occur with other conditions including epilepsy and intellectual disability (ID). Recent efforts to understand the genetic landscape of autism identified hundreds of genetic risk factors predisposing to autism including *de novo* single gene mutation (5-10%), copy number variations (CNVs) and chromosome anomalies (5%), and inherited single gene mutations (3%), although most cases (80-85%) have no known genetic cause.

Genetic risk factors can be either 'monogenic' where a single gene mutation is sufficient to predispose to autism or 'polygenic' where one mutation directly affects several genes simultaneously. CNVs are an example of the latter where chromosomal microduplication or microdeletion affect the gene dosage of multiple genes. The Simons Foundation Autism Research Initiative (SFARI) curates a list of ~1000 monogenic genetic risk factors of which 83 are categorised as the highest ranking (Categories 1 'high confidence' and 2 'strong candidates') indicating a robust

association between mutation in these genes and autism. SFARI lists 2240 CNVs associated with autism of which *16p11.2* microdeletion and microduplication are among the most frequent accounting for approximately 1% of cases. The *16p11.2* CNV comprises 27 protein coding genes so is a polygenic risk factor although it is currently unknown the extent to which each of the *16p11.2* genes are individual risk factors.

Autism manifests in early infancy and then persists into later life. A number of lines of evidence suggest that events during brain development *in utero* contribute to the subsequent development of symptoms (Packer, 2016). The developing cerebral cortex is comprised of three neuronal cardinal cell classes (progenitors, excitatory neurons, and inhibitory neurons) and three non-neuronal cardinal cell classes (astrocytes, oligodendrocyte precursors, and microglia). One important factor for cerebral cortex function is the balance between glutamatergic, excitatory principal neurons, which originate from progenitors located in the ventricular zone of the cerebral cortex, and inhibitory GABAergic interneurons (INs) which originate from progenitors located in the ganglionic eminences and then migrate into the cortex and integrate within functional circuits of the cortical plate (Hansen et al., 2013; Ma et al., 2013). Changes in the number, position, anatomy, or electrophysiology of inhibitory or excitatory neurons may perturb the excitatory/inhibitory balance (the E/I balance) and is hypothesised to be a convergent mechanism in autism and its co-occuring conditions (Bozzi et al., 2018; Nelson and Valakh, 2015; Puts et al., 2017; Rapanelli et al., 2017; Robertson et al., 2016) (Antoine et al., 2019)

The aim of the current study is to systematically identify types of cell in developing human cerebral cortex that are potentially vulnerable to autism risk factors using a single cell mRNA sequencing (scRNA-seq) dataset acquired from developing human foetal cortex spanning gestational weeks (GW) 8 to 26 (Zhong et al., 2018). While we found that some autism associated transcripts are differentially expressed between the cardinal cell classes our most striking finding was that a subset of differentiating INs first appearing at GW23 exhibited enriched expression of a strikingly high proportion of risk transcripts. This molecular analysis suggests the hypothesis that a large number of monogenic risk factors and the polygenic *16p11.2* microdeletion selectively target IN development resulting in IN phenotypes postnatally that contribute to autism and its comorbid conditions. We support this hypothesis using a *16p11.2*

microdeletion rat model where we identified hypersensitive electrophysiology and enlarged axon initial segment (AIS) phenotypes in somatostatin (Sst) expressing hippocampal INs.

METHODS.

Datasets

Three published cortical transcriptome datasets were used in this study to explore the gene expression pattern of autism-associated genes during cortical development.

The raw gene expression matrix in the scRNA-seq data of human foetal PFC was obtained from the Gene Expression Omnibus (GEO) under the accession number GSE104276, then the data was normalized as the original paper described (Zhong et al., 2018). We used the authors' original classification of six cardinal cell classes (NPC, ExN, IN, OPC, Astrocyte and Microglia).

The expression matrix of genes in the adult human cortical single nuclei RNA-seq data were downloaded under the accession number of GSE97930 (Lake et al., 2018). In the dataset from Lake et al., only cells that identified as "INs" were used for further analysis. The original eight interneuron clusters were grouped based on the expression pattern of marker genes (In1/2/3 as VIP, In4 as NG, In6 as PV, In7/8 as SST, Figure 2B,C in Lake et al., 2018).

For the mouse scRNA-seq datasets at of *Dlx6a-cre* fate-mapped cortical inhibitory neurons, the pre-processed Seurat objects were downloaded from the author's share link (https://www.dropbox.com/s/qe2carqnf9eu4sd/Filtered_Mayer-et-al.Rda.zip?dl=0) (Mayer et al., 2018). We used the authors' original classification of seven IN cell types (Sst, Pvalb, Vip, Id2, Nos1, Th and Igfbp6).

All three datasets were converted into Seurat objects by R package Seurat (version 2.3.0) for further analysis. In detail, in the dataset from Zhong et al., raw read counts were normalized based on the original paper described. Any cells with less than 1000 genes expressed were removed, and any gene expressed by less than 3 cells at less than 1 normalized expression value was removed. Pseudogenes, miRNA, rRNA, mitochondrial associated and ribosome related genes were excluded from further

124 analysis. The filtered gene expression matrix and the classification of the cardinal cell
125 classes were used to create a Seurat object. We also create a Seurat object for the
126 dataset from Lake et al. using the same procedure. The pre-processed Seurat object
127 from Mayer et al was not changed. The scRNA-Seq data was also analyzed with
128 BBrowser version 2.2.44 (SingleCell).

129 **Lists of autism risk genes**

130 Monogenic autism associated genes were downloaded from the SFARI database
131 (released May 2019) (https://gene.sfari.org/database/human-gene/) and the 83
132 highest ranking (SFARI 1+2) were analysed as these genes are significant statistically
133 in genome-wide studies between cases and controls. Besides these monogenetic
134 genes, the copy number variance (CNV) of genetic loci (CNV genes), either deletions
135 or duplications, are also linked to autism. We selected the 27 protein coding genes at
136 the *16p11.2* locus since both duplication and deletion of these genes has been linked
137 to significantly increased incidence of autism representing a potentially polygenic
138 cause of autism.

139 **Clustering and visualization of cell types**

140 The identification of six cardinal cell classes were obtained from the original paper and
141 re-plotted in a two-dimensional space of t-Distributed Stochastic Neighbor Embedding
142 (tSNE). In details, the highly variable genes (HVGs) were identified using Seurat
143 function FindVariableGenes. The mean of logged expression values was plotted
144 against variance to mean expression level ratio (VMR) for each gene. Genes with log
145 transformed mean expression level between 1 and 8, and VMR lower than 1.2 were
146 considered as highly variable genes. Then principal component analysis (PCA) was
147 performed with RunPCA function in Seurat using HVGs to analyze all the cells.
148 Following the PCA, we conducted JACKSTRAW analysis with 100 iterations to identify
149 statistically significant (p value < 0.01) principal components (PCs) that were driving
150 systematic variation. We used tSNE to present data in two-dimensional coordinates,
151 generated by RunTSNE function in Seurat, and the first 7 significant PCs identified by
152 JACKSTRAW analysis were used as input to RunTSNE function. Perplexity was set
153 to 20. t-SNE plot and the violin plot were generated using R package ggplot2.

154 We further clustered the three cardinal cell classes (NPC, ExN and IN) from the foetal
155 cortical dataset. Due to the different number of cells and the variant gene expression

156 pattern in each cardinal cell class, the HVGs were identified using the same method
157 but with the different parameters. For the cells in NPC, genes with log transformed
158 mean expression level between 0.5 and 8, and VMR lower than 1.2 were considered
159 as highly variable genes. For the cells in ExN and IN classes, genes with log
160 transformed mean expression level between 1 and 10, and VMR lower than 0.5 were
161 considered as highly variable genes. Then the statistically significant PCs were
162 calculated by JACKSTRAW analysis and used as input to get tSNE coordinates.
163 Clustering was done with Luvain Jaccard algorithm using t-SNE coordinates by
164 FindClusters function from Seurat. The resolution parameters used to IDENTIFY
165 clusters within the three cardinal cell classes were: NPC, resolution = 1; ExN,
166 resolution = 0.1; and IN, resolution = 0.5. Other parameters that we left at default.

167 **Identification of differential expressed genes**

168 All differential expression (DE) analyses were conducted using Seurat function
169 *FindAllMarkers*. In brief, we took one group of cells and compared it with the rest of
170 the cells, using Wilcoxon rank sum test. For any given comparison we only considered
171 genes that were expressed by at least 33% of cells in either population. Genes that
172 exhibit p values under 0.05, as well as log fold change over 0.33 were considered
173 significant. All heatmaps of DE analysis were plotted using R package pheatmap
174 (Figure 1C, Figure 3A and 3B, and Figure 5D).

175 **MetaNeighbor analysis**

176 MetaNeighbor analysis was performed using the R function MetaNeighbor with default
177 settings (Crow et al., 2018). The AUROC (Area under the Receiver Operating
178 Characteristic) scores produced by MetaNeighbor analysis indicate the degree of
179 correlation between cell clusters. Three gene lists were used as input to do
180 MetaNeighbor analysis among the 21 clusters of human foetal dataset: Highly variable
181 genes (HVGs) identified as significant differentialy expressed genes (DEGs) between
182 the clusters (Figure S2A); monogenic autism risk genes (Figure S2B); and*16p11.2*
183 genes (Figure S2C). The results from the MetaNeighbor analysis were plotted as a
184 heatmap using the gplots function heatmap. For a given gene set each pairwise
185 comparison between cell clusters is given an AUROC score ranging from 1.0 (red on
186 the heatmap) indicating that cells were highly probable to be of the same type to 0.0
187 (blue on the heatmap) indicating that it was highly improbable that the cells were of

188 the same type. A score on 0.5 (yellow on the heatmap) indicates that the gene set
189 used was unable to distinguish between the cells better than by chance.

190 **Projection based on multiple datasets**

191 We conducted canonical correlation analysis (CCA) and k-nearest neighbors analysis
192 (KNN) as we previous described to classify the cell types of foetal INs based on the
193 cell type features in the adult transcriptomics datasets (Mi et al., 2018). Briefly, we first
194 performed random forest analysis within HVGs to do feature selection for both foetal
195 and adult human cortical INs. Then we selected the shared HVGs between two
196 datasets that best represented the feature of IN cell types. The HVGs were used as
197 input gene list to RunCCA function, and the first 4 dimensions were used as input to
198 AlignSubspace function. The aligned projection vectors were used as input to do
199 dimensional reduction by RunTSNE function. Perplexity was set to 40. We used the
200 two t-SNE coordinates for adult cells to conduct KNN and re-assign foetal IN identities
201 using the knn.cv function from R package FNN. A foetal IN was assigned the identity
202 represented by the majority, and at least 5, of its closest 30 neighbours; in case of ties,
203 the cell remains unassigned. t-SNE plots, and the bar plots were generated using R
204 package ggplot2.

205 **Gene ontology analysis**

206 The resulting gene list, ordered by sign-adjusted P value, was the input for gene set
207 enrichment analysis to test for enriched gene ontology (GO) terms using the
208 clusterProfiler package version 3.4.4 with default settings. GO term analysis was
209 performed on three categories (Biological process. Molecular function. Cellular
210 component), and gene sets with a BH adjusted $P < 0.05$ were considered to be
211 significantly enriched. The top three significant GO terms in each category were
212 plotted by R package ggplot2.

213 **Animals**

214 All rats were bred in-house according to Home Office UK legislation and licenses
215 approved by the University of Edinburgh Ethical Review Committees and Home Office.
216 Animal husbandry was in accordance with UK Animals (Scientific Procedures) Act of
217 1986 regulations. Rat 16p11.2 DEL rat model (*16p11.2*$^{+/-}$) was generated by
218 CRISPR/Cas9 genome editing of the Sprague Dawley line (Qiu et al., 2019). Rats

219 were maintained on the Sprague Dawley background. P21 rat tissue was fixed by
220 transcardial perfusion with 4% paraformaldehyde in PBS, brains were then dissected
221 and immersed in 4% paraformaldehyde in PBS overnight at 4°C.

222 **In Situ Hybridisation and Immunofluorescence labelling**

223 Brains were cryoprotected in 30% sucrose in PBS, embedded in OCT and sectioned
224 at a thickness of 10µm using a cryostat (Leica, CM3050 S). Frozen sections were then
225 mounted on SuperFrost Plus™ slides (Thermo Fisher). *Gad1* In situ hybridisation on
226 frozen sections was performed as previously described (Wallace and Raff, 1999).
227 NeuN Immunofluorescence was performed following in situ hybridisation as described
228 previously (Clegg et al., 2014) with rabbit anti-NeuN (1/300, Abcam) Secondary
229 antibodies used were donkey anti-goat Alexa Fluor 488 and donkey anti-rabbit Alexa
230 Fluor 568 (both used 1/200 and from Life Technologies). Tissue was counterstained
231 using DAPI (1/1000, Life Technologies).

232 Axon initial segment (AIS) labelling, was performed as previously described (Oliveira
233 et al., 2020). Briefly, rats were perfused as described above, then post-fixed for 1 hour
234 at room temperature with 4% paraformaldehyde in 0.1 M phosphate buffer (PB).
235 Brains were then transferred to 0.1 M phosphate buffered saline (PBS) and 60 µm
236 thick coronal slices containing the CA1 region of hippocampus were cut on an
237 oscillating blade vibratome (Leica VT1000, Leica, Germany) and transferred to PBS.
238 Briefly, sections were rinsed in PBS then transferred to a blocking solution containing
239 10% normal goat serum, 0.3% Triton X-100 and 0.05% NaN_3 diluted in PBS for 1 hour.
240 Primary antibodies raised against AnkyrinG (1:1000; 75-146, NeuroMab, USA) and
241 somatostatin (Somatostatin-14, T-4102.0400; 1:1000, Peninsula Labs, USA) were
242 applied in PBS containing 5% normal goat serum, 0.3% Triton X-100 and 0.05% NaN_3
243 for 24-72 hours at 4 °C. Slices were washed with PBS and then secondary antibodies
244 applied (Goat anti-rabbit AlexaFluor 488 and Goat anti-mouse AlexaFluor 633,
245 Invitrogen, UK, both 1:500) in PBS with 3% normal goat serum, 0.1% Triton X-100 and
246 0.05% NaN3 added, overnight at 4°C. Sections were then washed with PBS, desalted
247 in PB, and mounted on glass slides with Vectashield® mounting medium (Vector Labs,
248 UK). Confocal image stacks of either the *str. pyramidale* or *str. oriens/*alveus border
249 were acquired on a Zeiss LSM800 laser scanning microscope equipped with a 63x
250 (1.4 NA) objective lens at 1024x1024 resolution (step size of 0.25 µm). Individual AIS

251 were measured offline using ImageJ as segmented lines covering the full extent of
252 AnkyrinG labelling observed. As in SSt INs the AIS often emerges from a proximal
253 dendrite, they were only identified where they emerged from a clearly fluorescent
254 labelled dendrite. A minimum of 25 AIS were measured from each rat.

255 For identification of somatostatin INs, slices were fixed following whole-cell patch-
256 clamp recording (see below) and fixed overnight in 4% PFA in 0.1 M PB.
257 Immunofluorescent labelling was performed according to the same protocol as above,
258 but excluding the AnkyrinG antibody. Secondary antibodies (goat anti-rabbit
259 AlexaFluor488, 1:500, Invitrogen, Dunfermline, UK) were applied with the added
260 inclusion of fluorescent-conjugated streptavidin (Streptavidin AlexaFluor 633, 1:500,
261 Invitrogen, Dunfermline, UK) to visualise recorded neurons.

262

263 **Imaging**

264 All fluorescence images were acquired using either a Leica AF6000 epifluorescence
265 microscope coupled to a Leica DFC360 digital camera running Leica LAS-X software,
266 or a Nikon Ti: E Inverted confocal microscope running Nikon NIS-Elements Confocal
267 software.

268

269 **NeuN/Gad1 Cell Quantification**

270 *Gad1*$^+$ and NeuN$^+$ cells within the cortex were quantified by counting *Gad1*$^+$ (red) and
271 NeuN$^+$ cells (green) within a 200µm wide column spanning the somatosensory cortex
272 (indicated region, Figure 5A). *Gad1*$^+$ and NeuN$^+$ cell position was quantified by
273 counting cells in 10 adjacent counting bins within the same 200µm wide column
274 spanning the somatosensory cortex.

275 *Gad1*$^+$ and NeuN$^+$ cells within the hippocampus were quantified by counting cells
276 within the *str. oriens* and *str. pyramidale* of the CA1 region (indicated region, Figure
277 5A). To control for the varying size of the counting area *Gad1*$^+$ cell number was
278 expressed as *Gad1*$^+$ cells per length (mm) of the CA1 region, length was measured
279 along the centre of the *str. pyramidale*. Gad1$^+$ cells were classified as belonging to *str.*
280 *pyramidale* if in contact with NeuN$^+$;*Gad1*$^-$ pyramidal cells, all other hippocampal

281 *Gad1*$^{+}$ cells superficial to this layer were classified as belonging to *str. oriens.* All
282 measurements and quantification was performed using FIJI software.

283

284 ***In vitro* slice electrophysiology***:*

285 Acute rat brain slices were prepared as previously described (Oliveira et al., 2021).
286 Briefly, rats were decapitated without anaesthesia and the brain rapidly dissected into
287 ice-cold sucrose-modified artificial cerebrospinal fluid (ACSF; in mM: 87 NaCl, 2.5 KCl,
288 25 $NaHCO_3$, 1.25 NaH_2PO_4, 25 glucose, 75 sucrose, 7 $MgCl_2$, 0.5 $CaCl_2$), which was
289 saturated with carbogen (95 % O2/5 % CO2). 400 µm horizontal brain slices were cut
290 on a vibratome (VT1200S, Leica, Germany) and transferred to sucrose-ACSF at 35°C
291 for 30 min and then room temperature until needed.

292 For whole-cell patch-clamp recordings slices were transferred to a submerged
293 recording chamber flowing with pre-warmed ACSF (in mM: 125 NaCl, 2.5 KCl, 25
294 $NaHCO_3$, 1.25 NaH_2PO_4, 25 glucose, 1 $MgCl_2$, 2 $CaCl_2$), bubbled with carbogen, and
295 perfused a rate of 4-6 $mL.min^{-1}$ at 30± 1 °C). Slices were viewed under infrared
296 differential inference contrast microscopy with a digital camera (SciCamPro,
297 Scientifica, UK) mounted on an upright microscope (SliceScope, Scientifica, UK) with
298 40x water-immersion objective lens (1.0 N.A., Olympus, Japan). Recording pipettes
299 were pulled from borosilicate glass capillaries (1.7 mm outer/1mm inner diameter,
300 Harvard Apparatus, UK) on a horizontal electrode puller (P-97, Sutter Instruments, CA,
301 USA), which when filled with a K-gluconate based internal solution (in mM 142 K-
302 gluconate, 4 KCl, 0.5 EGTA, 10 HEPES, 2 $MgCl_2$, 2 Na_2ATP, 0.3 Na_2GTP, 1
303 Na_2Phosphocreatine, 2.7 Biocytin, pH=7.4, 290-310 mOsm) which resulted in a 3-
304 5 MΩ tip resistance. Cells were rejected if: they were more depolarised than -50 mV,
305 had series resistance >30 MΩ, or the series resistance changed by more than 20%
306 during the recording. Recordings were performed with a MultiClamp 700B (Molecular
307 Devices, CA, USA) amplifier and filtered online at 10 kHz with the built-in 4-pole Bessel
308 filter and digitized at 20 kHz (Digidata1550B, Molecular Devices, CA, USA).)

309 Cells were identified either as CA1 pyramidal cells (CA1 PCs) with having large, ovoid
310 somata located in *str. pyramidale* and an apical dendrite entering *str. radiatum* or
311 somatostatin INs having bipolar, horizontally oriented somata at the *str. oriens*/alveus
312 border. All intrinsic membrane properties were measured in current-clamp. Passive

313 membrane properties, included resting membrane potential, membrane time constant,
314 and input resistance, were measured from hyperpolarising steps (-10 pA, 500 ms
315 duration), from resting membrane potential. Active properties were determined from a
316 series of hyper- to depolarising current steps (-500 to +500 pA, 500 ms) from a holding
317 potential of -70mV, maintained with a bias current injection. All AP properties were
318 determined from the first AP elicited above rheobase. Spontaneous EPSCs were
319 measured in voltage-clamp from a holding potential of -70mV and detected offline
320 based on a triexponential curve fit and a threshold of 3*SD of the baseline noise.
321 Traces were collected in pCLAMP 9 (Molecular Devices, CA, USA) and stored on a
322 desktop computer. Analysis of electrophysiological data was performed offline Stimfit
323 (Guzman, Schlögl, and Schmidt-Hieber 2014), blind to both genotype. All data from
324 somatostatin INs is shown only for those cells where clear immunofluorescent labelling
325 was detected at the level of the soma.

326 ***Statistics:***

327 All rat experiments and analyses were performed blind to genotype, which were
328 sampled in a random manner between experimental days. All data shown as mean ±
329 standard error of the mean (SEM), with the number of cells (n) and animals (N)
330 indicated where appropriate. All electrophysiology data are reported as cell averages.
331 All histology data (AIS lengths and cell counts) are shown as animal averages.
332 Minimum sample size was calculated based on our previous effect size for cellular
333 hyperexcitability and AIS length (Booker *et al*., 2020), assuming 80% power to
334 determine 95% probability of rejecting the null-hypothesis. Statistical comparisons
335 were performed using a linear mixed-effect model (or its generalised form) using the
336 *lme4* package in R (Bates *et al*., 2015), with genotype or cell-type as fixed effect, with
337 slice/animal/litter included as random effects. Based on the linear mixed-effects model,
338 p-values for statistical effects were tested using the Wald test, based on effect size
339 and variance determined from the relevant mixed-effects model. For experiments
340 examining the density of interneurons and principal cells, animal average densities
341 were the principal replicate which was tested with 2-way ANOVA. Statistical
342 significance was assumed if $p<0.05$.

343

344

345 **RESULTS.**

346 **Differential expression of autism risk genes among foetal cortical cardinal cell**
347 **classes**

348 A general supposition is that functional disruption of a gene will more likely affect the
349 cells expressing high levels of it's transcript. Based on such a principle, a cell type
350 expressing high levels of an autism associated transcript is regarded as potentially
351 vulnerable to genetic mutation in that gene with the resulting cellular phenotype
352 contributing to the development of autism. Accordingly, we have calculated differential
353 expression of autism associated transcripts among cell types in foetal human cerebral
354 cortex to identify cells potentially vulnerable to autism genetic risk factors during brain
355 development.

356 We started with a scRNA-seq dataset comprising 2306 cells taken from human foetal
357 pre-frontal cortex spanning gestational weeks (GW) 8 to 26 (Zhong et al., 2018). Six
358 cardinal cell types were identified in the authors' original classification, including neural
359 progenitor cells (NPCs), excitatory neurons (ExN), interneurons (IN), oligodendrocyte
360 precursor cells (OPCs), astrocytes, and microglia (Fig. 1A,B and Fig. S1A,B).
361 Differentially expressed genes (DEGs) were calculated across these six cardinal cell
362 classes. Based on the DEGs, we find that the six cell classes showed distinct cardinal
363 class aggregation and specific gene expression profiles associated with neural
364 progenitor cells (NPC), excitatory neurons (ExN), inhibitory neurons (IN),
365 oligodendrocyte precursors (OPC), astrocytes, and microglia. A list of well-known cell
366 class markers that are included in the DEGs was used to illustrate the classification
367 across six cardinal cell classes (Nowakowski et al., 2017, Pollen et al., 2014, Camp et
368 al., 2015) (Fig. 1B). The markers used to identify different cardinal cell classes were:
369 *PAX6*, *HES2* and *VIM* (NPCs); *NEUROD2*, *NEUROD6* and *RBFOX1* (ExNs); *GAD1*,
370 *GAD2*, *DLX1* and *DLX2* (INs); *OLIG1*, *OLIG2* and *COL20A1* (OPCs); *GFAP*, *AQP4*
371 and *SLCO1C1* (astrocytes); *PTPRC* and *P2RY12* (microglia). The expression pattern
372 of these marker genes show that the cardinal cell classes were correctly represented
373 in our analysis (Fig 1B).

Figure 1

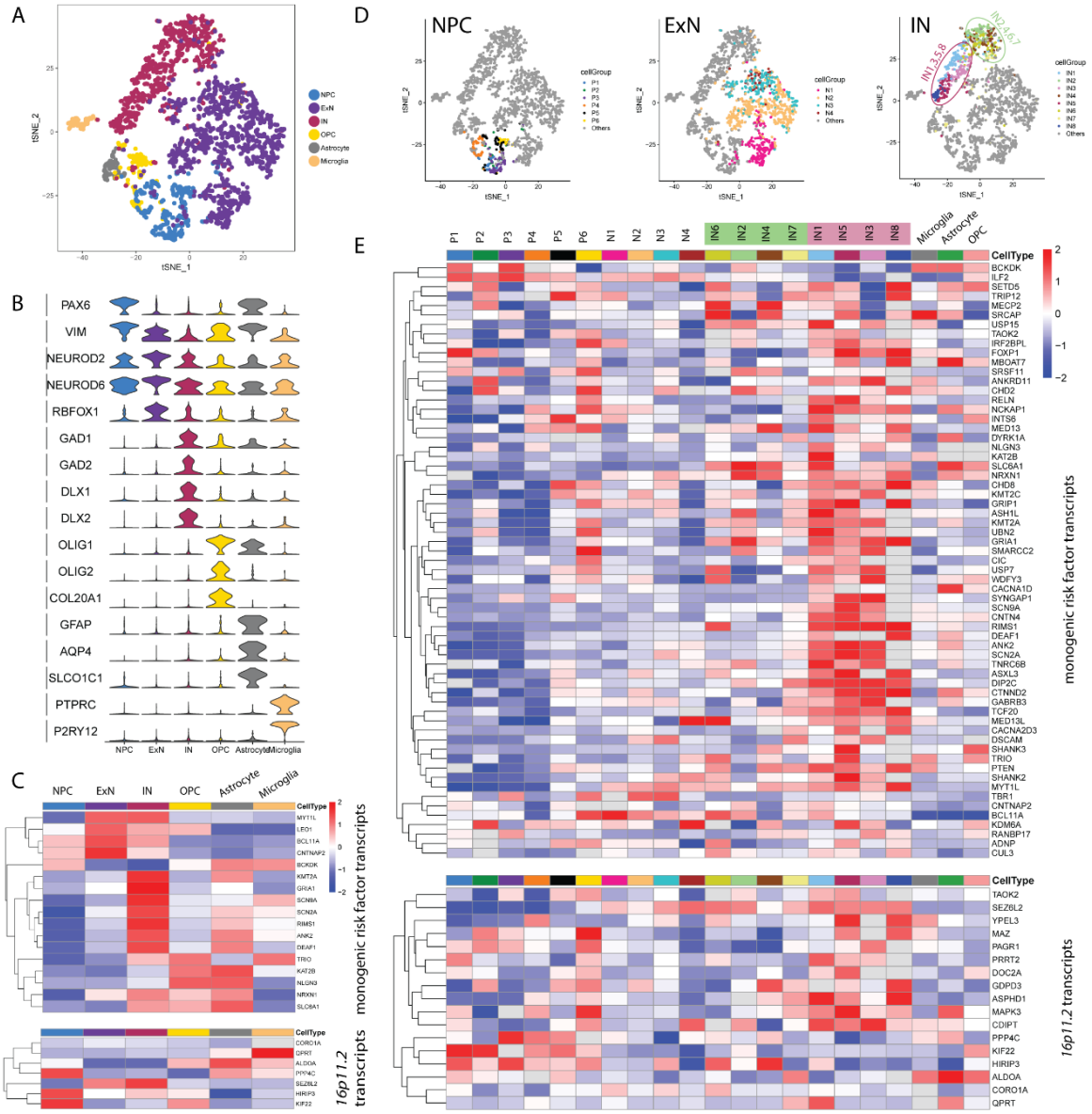

Figure 1: (A-C) Differentially expression of autism risk factor transcripts among foetal cortical cardinal cell classes. (A) *t*-SNE plot showing the cardinal cell classes identified in the dataset. (B) Violin plot illustrating the expression pattern of marker genes among the six cardinal cell classes. (C) Heatmap illustrating the expression pattern of significantly differentially expressed autism risk factor transcripts across cardinal cell classes (Wilcox test, adjust $p < 0.05$, log (fold change) > 0.3). Top: monogenic autism risk factor transcripts; Bottom: *16p11.2* transcripts. (D,E) Unsupervised clustering within the cardinal classes and similarity comparison between cell clusters. (D) Unsupervised clustering subdividing the cardinal classes into 21 different cell clusters. OPC, astrocytes, and microglia were not further clustered. (E) Heatmap illustrating the

385 expression pattern of differentially expressed autism risk factor transcripts across 21
386 cell clusters (Wilcox test, adjust $p < 0.05$, log (fold change) > 0.3) for differentially
387 expressed monogenic autism risk factor transcripts (top panel) and differentially
388 expressed *16p11.2* transcripts (bottom panel).

389 Then we identified the expression pattern of autism risk factor transcripts across the
390 cardinal cell classes and found that 17/83 high confidence and strong candidate
391 monogenic risk factor transcripts and 7/27 *16p11.2* transcripts were significantly
392 differentially expressed between cardinal cells classes (Fig 1C). A heatmap of
393 expression of the monogenic autism risk factor transcripts (Fig 1C – top) and the
394 *16p11.2* transcripts (Fig 1C – bottom) shows expression of each autism risk factor
395 transcript (rows) in each of the six cardinal cell classes (columns). Transcript levels
396 with expression greater than average across the cardinal classes are shown in red,
397 while transcripts with lower than average expression are shown in blue. There was no
398 obvious pattern to suggest that any cardinal class was particularly vulnerable to a large
399 proportion of either monogenic autism genetic risk factors.or the *16p11.2*
400 microdeletion.

401

402 **Identification of human foetal INs potentially disproportionately vulnerable to**
403 **genetic autism risk factors.**

404 The single-cell approach allows us to investigate the variability of highly expressed
405 genes among molecularly defined cell subpopulations and identify cells within cardinal
406 classes which may be vulnerable to genetic autism risk factors. Based on
407 unsupervised clustering, we subdivided the cardinal classes into 21 different cell
408 clusters (Fig. 1D): 6 for NPCs (P1-6); 4 for ExNs (N1-4); and 8 for INs (IN1-8). The
409 non-neuronal cardinal cell classes (OPC, astrocytes, and microglia) contained small
410 numbers of tightly clustered cells and were not further subdivided.

411 We clustered the 21 clusters according to transcriptomic similarity using
412 MetaNeighbour analysis with ~2000 highly variable genes (Fig. S2A) and used this
413 ordering to generate a heatmap of the 62/83 monogenic risk factor transcripts (Fig.
414 1E, top) and 17/27 *16p11.2* transcripts genes (Fig. 1E, bottom) that were significantly
415 differentially expressed between clusters. Violin plots of all autism risk transcripts
416 (including those not differentially expressed between clusters) for the 83 monogenic

417 autism risk transcripts (Fig. S3A) and 27 *16p11.2* transcripts (Fig. S3B) show the
418 expression profile in each cluster.

419 Of the differentially expressed monogenic risk factor transcripts (Fig 1E, top) a few
420 were enriched in progenitor cells, (for example *IRF26PL*, *BCL11A*, and *CHD2*), with
421 fewer transcripts enriched in excitatory neurons (for example *TBR1*). Other transcripts
422 were expressed across many clusters (for example *KMT2A, ILF2, SMARCC2,*
423 *SRSF11, UPF3B, TNRC6B*), while others showed relatively low expression across cell
424 types (for example *GRIN2B, MAGEL2, and MET*). A striking feature of the heatmap
425 was a preponderance of relatively high gene expression (red shading) in the IN cell-
426 types (for example *SCN2A*, *SCN9A, DEAF1, SHANK2, RIMS1, GRIP1, SYNGAP1*),
427 which was most apparent for the IN subgroups IN1,3,5,8 (purple highlight in Fig. 2E
428 and circle in Fig. 1D) compared to IN2,4,6 7 (green highlight in Fig. 2E and circle in
429 Fig. 1D) and other clusters.

430 We observed a similar pattern for *16p11.2* transcript expression (Fig 1E, bottom) with
431 a preponderance of high expression in IN clusters1,3,5,8, indicating specifically
432 enriched expression of subset of *16p11.2* transcripts (for example *SEZL6L2*, *PRRT2*,
433 *QPRT*, and *YPEL3*) with the next highest number of enriched transcripts in progenitor
434 clusters (for example *KIFF22* and *PPC4C*). Other transcripts are expressed both in
435 progenitors and INs but much less in excitatory neurons (for example *MAPK3*), and
436 others broadly across all cell clusters (for example *TMEM219*) or at very low levels in
437 any cluster (*ASPHD1*, *C16orf54*, *C16orf92*, *SPN*, *TBX6*, *ZG16*).

438 To investigate how well the expression of autism risk factor transcripts defined the cell
439 clusters more systematically we used MetaNeighbor analysis which reports on how
440 similar cells are to each other based on expression of a given input gene set using
441 AUROC scores (Crow et al., 2018). From this, we generated a pairwise comparison
442 matrix between the 21 cell clusters (Fig. S2). Performing MetaNeighbor with the same
443 ~2000 DEGs used to perform hierarchical clustering (Fig. S2A) we confirmed that cells
444 in each cardinal class were generally more similar within class (red on heatmap) and
445 less similar (blue on heatmap) between cardinal classes. Nevertheless, some neurons
446 (N1 and N2) were quite similar to progenitors (P1-P6) likely indicating that they
447 represented relatively immature excitatory neurons that retained some progenitor
448 identity. Within the INs there was a clear divide between IN1,3,5,8 (red box in Fig.

449 S2A-C) and IN2,4,6 (green box in Fig. S2A-C) cluster groups, with highest similarity
450 within group and low similarity between groups. Next, we performed the same analysis
451 for the 83 SFARI monogenic autism risk factor transcripts (Fig. S2B) and found that
452 strongest similarity was retained within the progenitor group P1-P6 and the IN group
453 IN1,3,5,8. A similar pattern emerged when we used the 27 *16p11.2* transcripts as the
454 gene-set (Fig. S2C), although here the strongest similarity was within the progenitor
455 group P1-6 and between IN5 and IN8. These results indicate that the immature INs
456 can be robustly distinguished from other cells in the developing brain by their
457 expression pattern of autism risk factor transcripts.

458 We conclude from the gene expression analysis that a subset of developing INs,
459 IN1,3,5,8, in GW8-26 human foetal cerebral cortex express a high proportion of autism
460 associated transcripts at higher levels than other cells. This suggests that IN1,3,5,8
461 are vulnerable, and in some instances selectively vulnerable, to a large number of
462 independent monogenic genetic autism risk factor and *16p11.2* microdeletion during
463 cerebral cortex development.

464

465 **Properties of human foetal INs potentially vulnerable to autism risk factors.**

466 Having identified IN1,5,3,8 as a potentially important class of INs targeted by genetic
467 autism risk factors we next examined their developmental and transcriptional
468 properties. We found that very few IN1,3,5,8 INs were present during the earlier stages
469 (GW8-19) of cerebral cortex development, typically appearing from GW23 and with
470 the vast majority of IN1,5,3,8 INs present at GW26 (Fig. 2A). On the other hand,
471 IN2,4,6,7 clusters contained higher proportions of cells from earlier stages (Fig. 2A),
472 suggesting that IN1,3,5,8 might represent a more mature state than the rest of IN
473 clusters in our dataset. INs have reached the cortex in substantial numbers by GW16
474 (Fig. S1B) indicating that IN1,3,5,8 cells correspond to a stage of the developmental
475 trajectory after tangentially migrating INs enter the cortex (Hansen et al., 2013; Ma et
476 al., 2013).

Figure 2

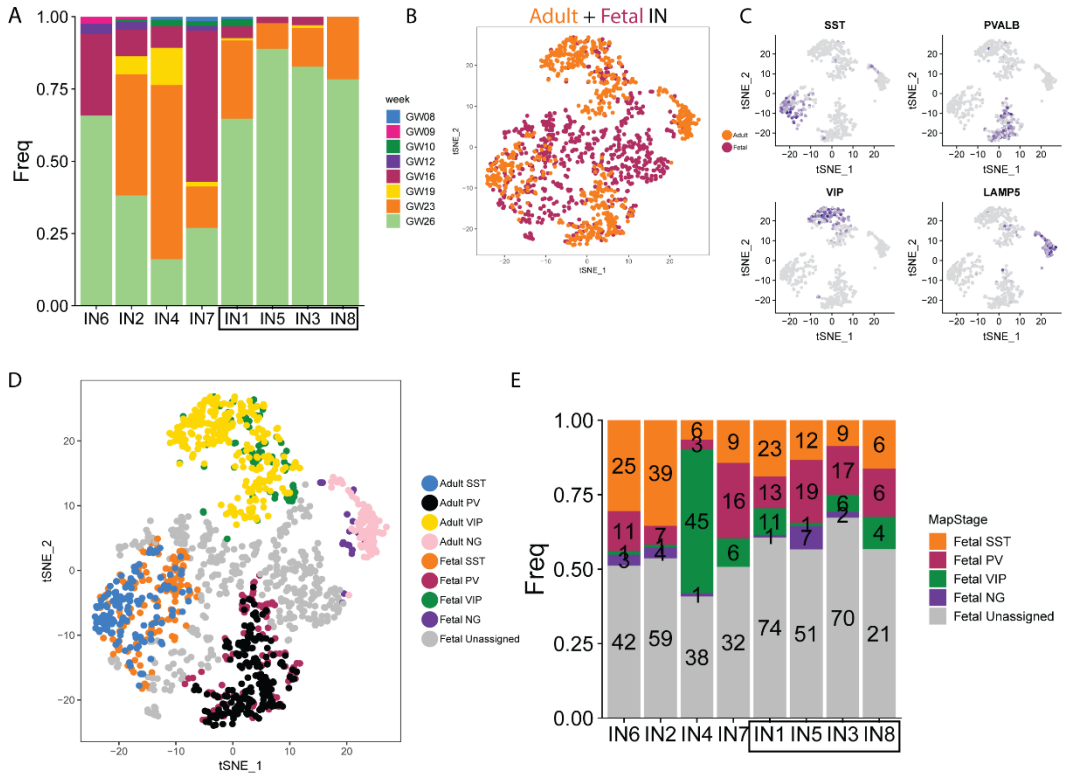

Figure 2: (A) Bar plot depicting the proportion of sample ages in each IN cluster. **(B)** Canonical correspondence analysis (CCA) integrating the foetal and adult human scRNA-seq data. **(C)** CCA-KNN analysis in t-SNE space provides a method to categorise immature INs into SST, PV, VIP and Neuroglia form (NG) classes according to their transcriptomic similarity to mature neurons from human adult cortex. **(D)** Gradient plots showing gene expression pattern of marker genes of IN lineages in t-SNE space. **(E)** Bar plot depicting the number and proportion of IN cell types in each IN cluster.

We used canonical correlation analysis (CCA-KNN) to integrate foetal (Zhong et al., 2018) and mature (Lake et al., 2018) human IN scRNAseq datasets to identify mature cell types corresponding to developing IN1,3,5,8 clusters. We first reduced the dimensionality of both datasets (adult IN cells = orange; foetal IN cells = blue) onto the same two-dimensional space using *t*-SNE (Fig. 2B), which allowed the identification of 4 major cell types of adult INs based on the expression of variable genes shared between both datasets. We then assigned identities to adult based on expression of

markers for PV, SST, VIP and neurogliaform cells illustrated by gradient plots of *SST*, *PVALB*, *VIP* and/or *LAMP5* transcripts to identify defined classes of cortical INs (Fig. 2C). This then allowed us to assign foetal INs to each of these cell types based on transcriptional similarity to the mature INs (Fig. 2D). Of the IN1,3,5,8 cells classified in this manner we found that they were not homogenous, but rather consisted of PV, SST, and VIP cell types (Fig. 2E). A parsimonious interpretation is that the foetal IN1,5,3,8 are cells destined to become several categories of mature IN cell types, although this awaits further investigation as assignation of cell lineage from scRNA-seq data is ambiguous.

To gain further insight into the identity and developmental cell state represented by IN1,3,5,8, we first performed differential expression analysis with respect to other INs (Fig. 3A) and used the genes enriched in IN1,3,5,8 with a log fold change higher than 3 (1623 genes FDR < 0.001) to test for Gene Ontology (GO, biological process) enrichment. We found that within the top 30 GO terms (ordered according to Fold Enrichment), 9 categories were related to synaptic plasticity, synaptic maturation and synaptic transmission and 6 categories were related to neuron projection and growth (Fig. 3B), with fold enrichments ranging from 6 to 10, suggesting that IN1,3,5,8 cells show earlier maturation of neurites and synapses than other INs. The Gene Ontology term “Regulation of Synaptic Plasticity” contains 192 genes, from which 54 are differentially expressed in IN1,3,5,8. A closer inspection of the expression pattern in the t-SNE space showed that many of these genes followed a general expression level gradient trend with its maximum levels in INs corresponding to IN5 and IN8 (*MEF2C*, *ADCY1*, and *SYT4* shown as examples in Fig. 3C). This suggested that the INs in the dataset must be ordered in the t-SNE space according to a gradient of synapse formation, with IN5,8 being the higher extreme of this axis. To confirm this, we performed differential expression analysis between IN5,8 IN cells versus all other INs (Fig. 3D) and found a high enrichment of synaptic plasticity-related terms but this time showing fold enrichments ranging from 7 to 20 (Fig. 3E), almost doubling the values of the previous comparison.

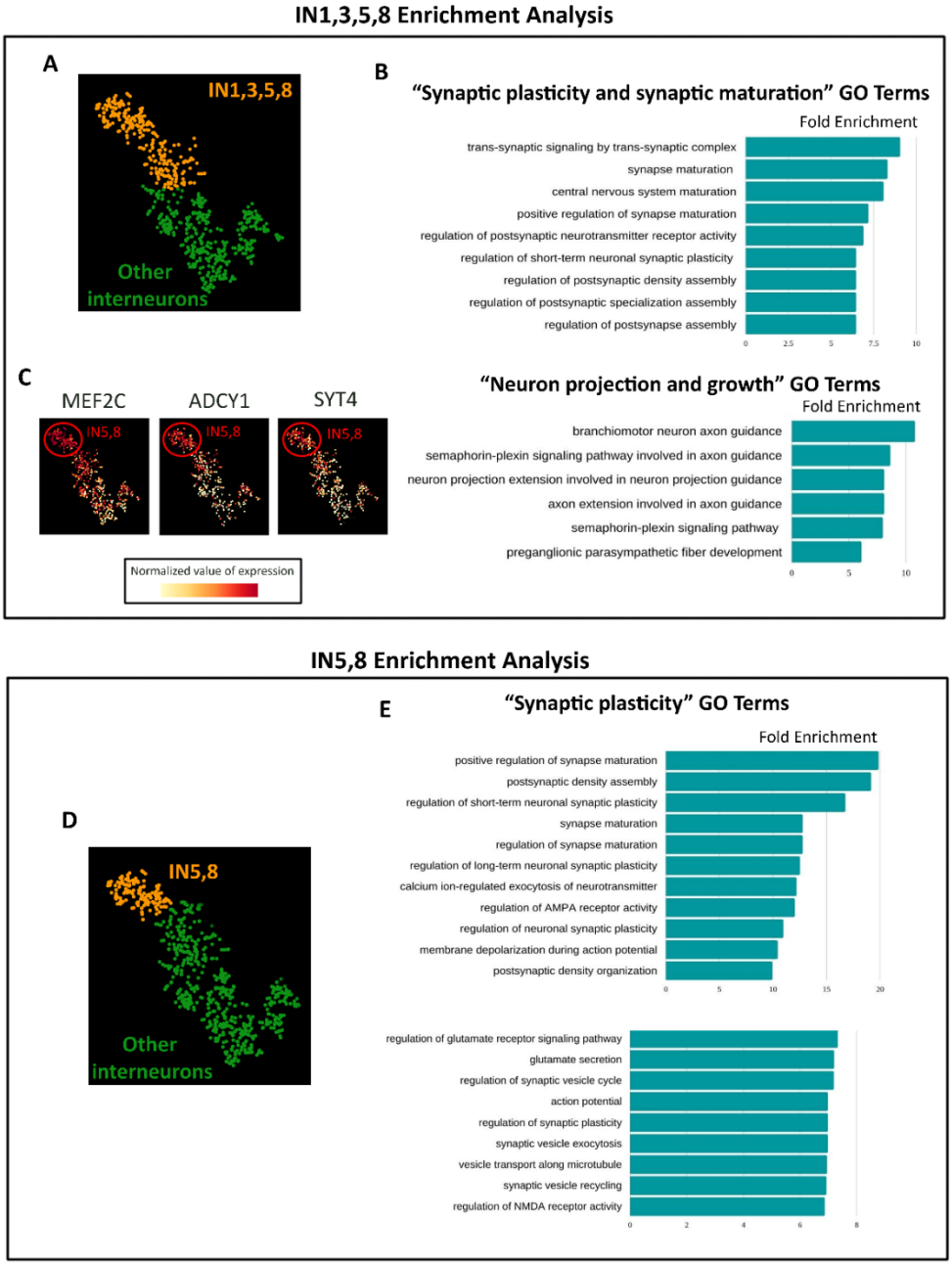

Figure 3. Characterisation of INs by gene ontology analysis (A-C) Gene ontology (GO) analysis in IN1,3,5,8 (orange in A) versus other INs (green in A) reveals enrichment of GO terms associated with (B) synaptic maturation and plasticity and axon extension and guidance. (C) gradient plots of MEF2C, ADCY1, and SYT4 showing that these transcripts are expressed in a gradient across INs with highest expression in IN5,8. (D,E) Gene ontology (GO) analysis in IN5,8 (orange in D) versus other INs (green in D) reveals enrichment of GO terms associated with (E) synaptic maturation and plasticity.

533 Finally, to gain further insight into IN5,8 neuronal identity, we compared IN5,8 cluster
534 versus all other neurons (including both excitatory and inhibitory, Fig. S4A).
535 Interestingly, enriched functional terms were mainly related to synaptic plasticity,
536 learning and social behaviour (Fig. S4B). Visual inspection of gradient plots in the t-
537 SNE space confirmed that many of the genes linked to synaptic plasticity and
538 maturation are selectively expressed in IN5,8 (Fig. S4C). Together this analysis
539 suggests that IN1,3,5,8 are relatively differentiated INs elaborating processes and
540 forming synapses.

541 This raises the possibility that by targeting the stage of the IN developmental trajectory
542 represented by IN1,3,5,8, multiple genetic autism risk factors perturb the development
543 of the physiological properties of foetal INs. The remaining interneurons IN2,4,6,7
544 appear less vulnerable and may represent an earlier stage in the IN developmental
545 trajectory or correspond to different IN lineages. Either way our analysis suggests
546 genetic autism risk factors impact on many INs during foetal development and may
547 affect their function into postnatal life.

548

549 **Conservation of potentially vulnerable INs between humans and rodents.**

550 These analyses of human foetal neurons suggest the testable hypothesis that a large
551 proportion of autism related genes selectively regulate IN development in the human
552 foetal cortex. A prediction of this hypothesis is that there will be IN phenotypes initiated
553 during human brain development *in utero* that persist into postnatal life and predispose
554 to autism and its comorbid conditions. Such investigation is currently not possible,
555 however, rodent models provide a complementary means to test cellular vulnerability
556 to autism genetic risk factors under physiological conditions. As such, we next
557 confirmed that developing rodent brain contains INs with similar molecular properties
558 to the potentially vulnerable human foetal INs IN1,3,5,8 identified above.

559 We identified two mouse scRNAseq data sets comprising FACS sorted cortical INs at
560 embryonic day (E) 18.5 and postnatal (P) day 20, when INs are differentiating and
561 forming circuits (Mayer et al., 2018). For each mouse developmental stage we used
562 CCA-KNN to integrate the mouse and human INs into the same tSNE space (Fig. 4
563 A,D) to allow us to identify mixed clusters of transcriptomically similar mouse and
564 human INs (Fig. 4B,E).

Figure 4

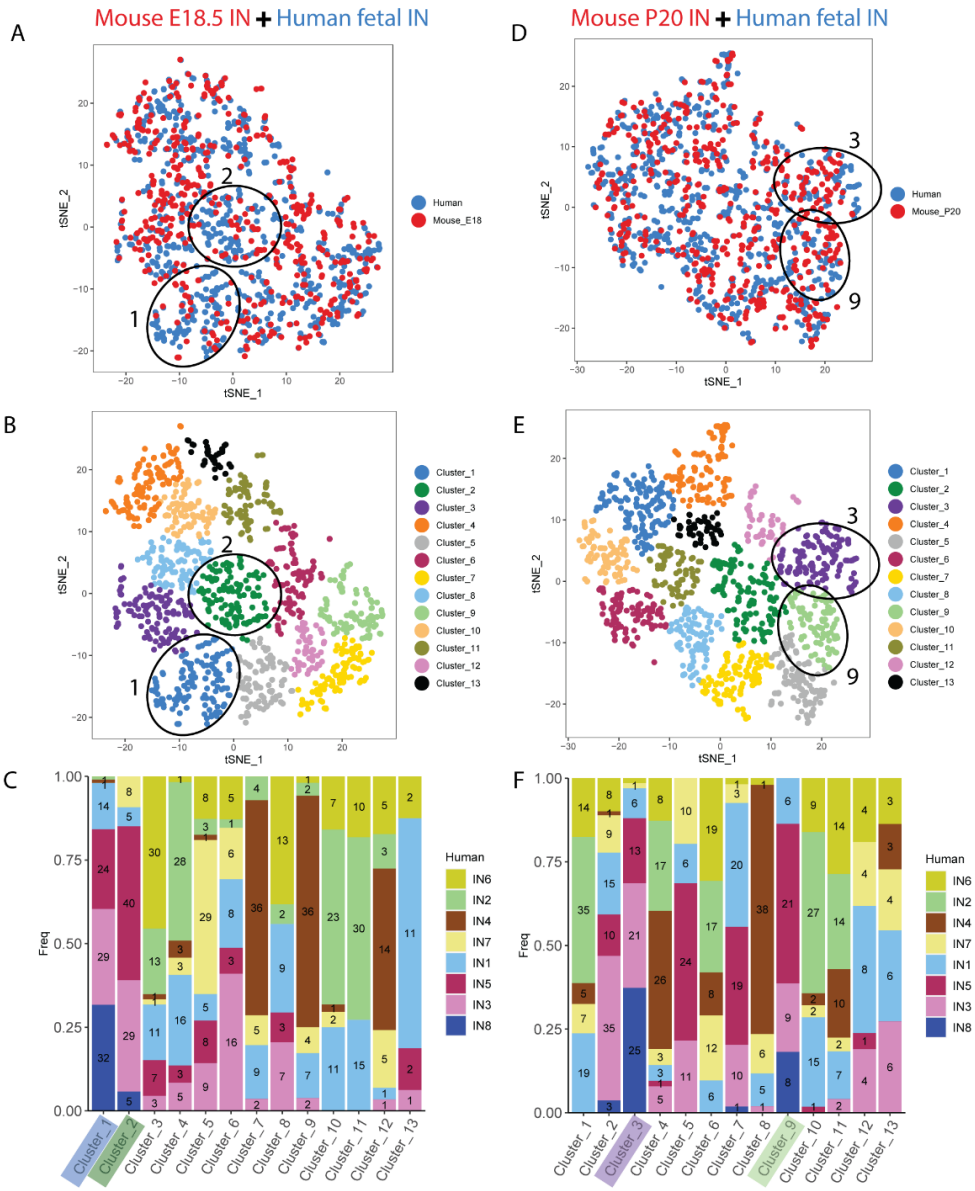

Figure 4: Identifying transcriptomic correlates between developing human and mouse INs at (A-C) E18.5 and (D-F) P20. (A,D) CCA integration of mouse (red) and human (blue) INs in tSNE space. (B,E) JACCARD clustering into 13 mixed clusters. (C,F) Distribution of human IN1-8 INs in each of the mixed clusters with numbers of cells shown within each bar. The mixed clusters 1&2 for E18.5 (A-C) and 3&9 for P20 (D-F) that are most enriched for human IN1,3,5,8 cells are indicated on each panel.

For each mouse developmental stage, we examined how the human IN cell types IN1-8 were distributed between the mixed mouse+human clusters (Fig. 4C,F). This

574 analysis revealed that E18.5 clusters 1 and 2 (indicated in Fig 4A-C) and P20 clusters
575 3 and 9 (indicated in Fig 4D-F) contained the greatest enrichment of human IN1,3,5,8
576 cells. Critically, these clusters contained comparable numbers of mouse and human
577 cells indicating that the developing and postnatal mouse possesses INs molecularly
578 similar to human IN1,3,5,8 cells. These findings suggest that INs we have identified
579 as potentially vulnerable to genetic autism risk factors are shared between humans
580 and rodents allowing us to investigate them under physiological conditions using
581 rodent models.

582

583 **Changes to IN function in the rat model of *16p11.2* microdeletion.**

584 The *16p11.2* microdeletion causes *16p11.2* transcript levels to be reduced by about
585 50% in humans and rodent models (Tai et al., 2016) (Pucilowska et al., 2015) (Horev
586 et al., 2011) (Blumenthal et al., 2014). As multiple *16p11.2* transcripts are normally
587 highly enriched in developing INs (Fig. 1), we hypothesised that their simultaneous
588 reduced expression following *16p11.2* microdeletion may synergistically impact IN
589 development with post-natal consequences on IN phenotypes. We next set out to test
590 this hypothesis by performing electrophysiological and anatomical interrogation of the
591 rat *16p11.2* microdeletion model (*16p11.2*$^{+/-}$ rats).

592 As *16p11.2* transcripts are expressed in the ganglionic eminences where IN
593 progenitors reside (Morson et al., 2021), we first asked if the numbers of inhibitory
594 and/or excitatory neurons populating the cortex post-natally was different in the
595 *16p11.2*$^{+/-}$ rats. To investigate this, we counted these cardinal cell classes in WT and
596 *16p11.2*$^{+/-}$ rats at postnatal day (P) 21, an age by which INs have migrated into the
597 cortex and assumed their final laminar positions forming circuits with resident
598 excitatory neurons. We combined immunostaining for the pan-neuron-specific marker
599 NeuN and *in situ* hybridization for the IN marker *Gad1* to identify NeuN^{+};*Gad1*$^{-}$
600 excitatory neurons and NeuN^{+};*Gad1*$^{+}$ INs in the cortex (Fig. 5A). Quantification within
601 a 200µm wide column spanning the somatosensory cortex and hippocampus (shown
602 figure 5A) shows no significant difference between WT and *16p11.2*$^{+/-}$ rats in total IN
603 number ($t_{(8)}$ = 0.27, p = 0.80 t test, Figure S5A) or in the proportion of the neuronal
604 population identified as inhibitory or excitatory ($t_{(8)}$ = 0.15, p = 0.89 t test, Fig. S5B). To
605 assess whether the cortical laminar position of INs was altered in *16p11.2*$^{+/-}$ rats we

606 quantified IN and excitatory neuron number in 10 adjacent counting areas spanning
607 the somatosensory cortex. We found no significant change in the distribution of INs
608 across the cortex (Figure 5B), nor did we see any change in the inhibitory/excitatory
609 proportion in any counting area (Fig. S5B). Next, we examined IN number and position
610 in the CA1 region of the hippocampus. Total combined IN number within the *str. oriens*
611 (SO) and *st. pyramidale* (SP) of CA1 was unchanged between WT and *16p11.2*$^{+/-}$ rats
612 ($t_{(8)}$ = -0.09, p = 0.93 t test, Fig. S5A). Total IN number within the SO and SP was also
613 unchanged indicating that the position of INs within the hippocampus is unaffected in
614 *16p11.2*$^{+/-}$ rats (Figure 5C). These data indicate that the *16p11.2* microdeletion does
615 not have a major impact on number or distribution of inhibitory or excitatory neurons
616 in the cerebral cortex or CA1 INs post-natally.

617 Our bioinformatic analysis indicated that human foetal IN1,3,5,8 cells contribute to
618 mature somatostatin (SST) INs (Fig 2E). As such, we next asked whether the *16p11.2*
619 microdeletion might have an effect on SSt IN development to alter their physiological
620 properties. To test this, we performed whole-cell patch-clamp recordings from
621 identified SSt INs and local pyramidal cells (PCs) in the CA1 region at P21.

622 We performed recordings from identified INs that expressed SSt in CA1 of the
623 hippocampus, which also show expression of PV in parvalbumin (PV) in 50% of cells
624 (Booker and Vida, 2018). The recorded Sst INs predominantly had horizontally
625 oriented dendrites in *str. oriens,* which when present had an axon extending into *str.*
626 *lacunosum-moleculare* (Booker and Vida, 2018). In the present study, we recorded
627 from 30 WT (from 15 rats) and 28 *16p11.2*$^{+/-}$ (10 rats) SSt INs, which all displayed clear
628 immunoreactivity for the SSt neuropeptide at the somata. In response to
629 depolarisingcurrent injections (0-500 pA, 100 pA steps, Fig. 5D), SSt INs generally
630 responded with high action potential discharge rates, which had a peak action potential
631 discharge of 27.4 ± 2.5 action potentials/500 ms (Fig. 5E). We found that SSt INs from
632 the *16p11.2*$^{+/-}$showed elevated action potential discharge, compared to WT controls
633 ($F_{(5,\ 58)}$=5.10,P=0.0006 for interaction of genotype and current, N=15 WT and 10
634 *16p11.2*$^{+/-}$ rats, Fig. 5E), indicating cellular hyperexcitability. Comparison of the
635 intrinsic physiology of SSt INs revealed a general 17% reduction of rheobase current
636 in 16p11.2$^{+/-}$ compared to WT rats, albeit not significantly so (p=0.1087 LME, Fig. 5F),
637 this was accompanied by a 6% hyperpolarisation of the voltage threshold (p=0.0279

638 LME, Fig. 5G). All other physiological parameters were similar between genotypes
639 (Supplementary Table S1).

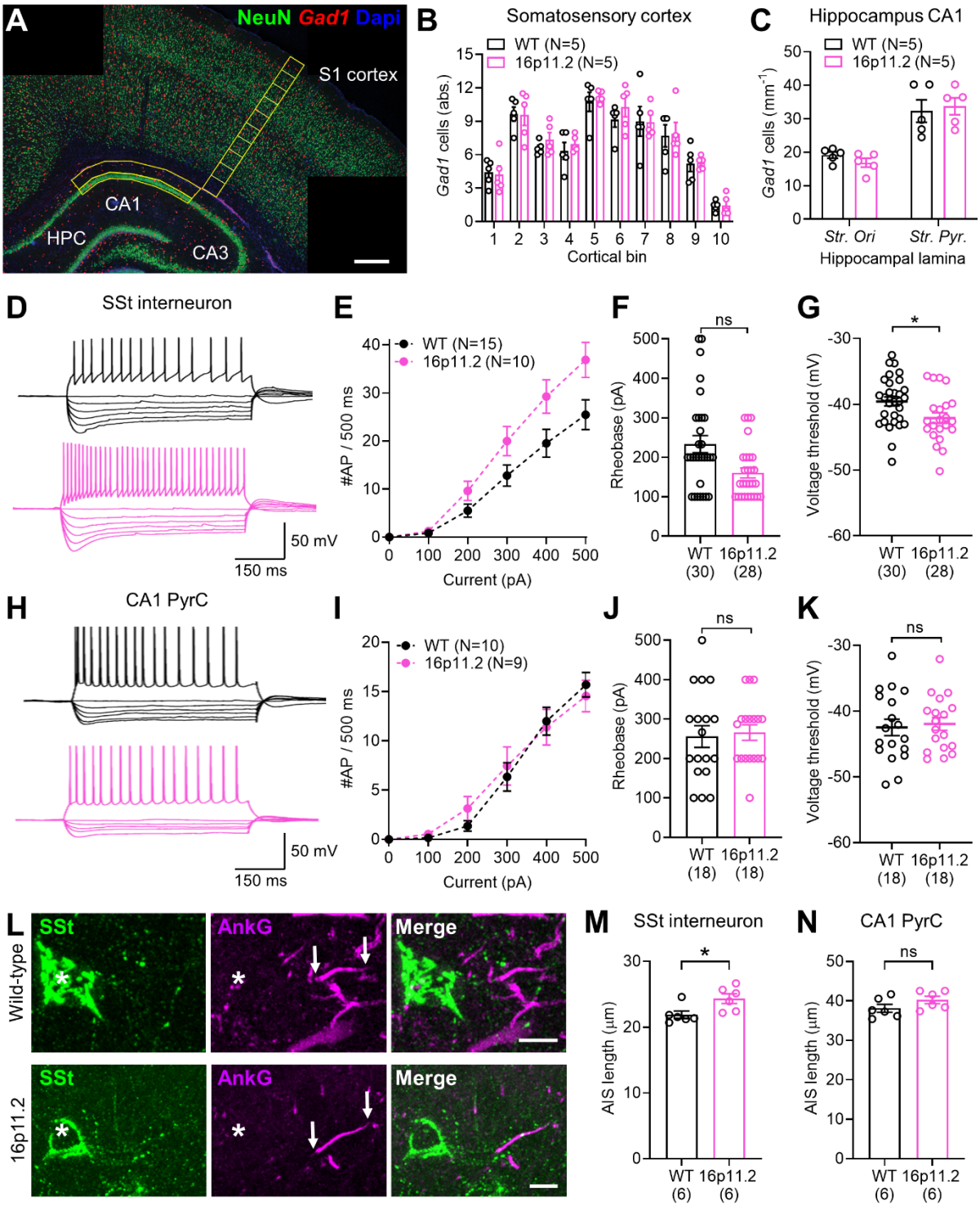

640

641 **Figure 5. Selective hyperexcitability of SSt INs in *16p11.2*$^{+/-}$ rat hippocampus, but**
642 **with no change in IN number. (A)** Overview micrograph of *Gad1* mRNA and NeuN
643 protein expression in the rat hippocampus and cortex at P21. Gad1 expressing INs

644 (red) and NeuN expressing, Gad1 negative excitatory neurons (green) can be
645 observed in the cortex and hippocampus. Scale bars 400µm **(B)** Quantification of
646 *Gad1*-positive IN (IN) number through the somatosensory cortex in WT (black, n=5)
647 and 16p11.2$^{+/-}$ (pink, n=5) rats. Counting areas indicated yellow in A with cortical bins
648 numbered from 1 at the ventricular edge to 10 at the pial surface. **(C)** Quantification of
649 the combined total number of *Gad1*-positive neurons in the s*tr.oriens* (*Str. ori*) and s*tr.*
650 *pyramidale* (*Str pyr.*) of the CA1 region of the hippocampus in WT (N=5) and 16p11.2$^{+/-}$
651 (N=5)rats. Counting area indicated in **A**. (**D**) Representative action potential discharge
652 in response to hyper- to depolarising current steps in putative SSt-INs, from the *str.*
653 *oriens* of CA1 from WT (top) and 16p11.2$^{+/-}$ rats (bottom). **(E)** Summary current-
654 frequency plots from identified SSt INs from WT (N=15 rats) and *16p11.2*$^{+/-}$ (N=10
655 rats). (**F**) Quantification of rheobase current in identified SSt-INs from WT (n=30 cells)
656 and *16p11.2*$^{+/-}$ (n=28 cells) rats. (**G**) Measurement of the voltage threshold of the first
657 action potential elicited at rheobase for the same cells in **F**. (**H-K**) the same analysis
658 performed in CA1 pyramidal cells from WT (N=10 rats, n=18 cells) and *16p11.2*$^{+/-}$ (N=9
659 rats, n=18 cells). (**L**) Representative micrographs showing immunohistochemical
660 labelling for SSt (green), the AIS marker AnkyrinG (AnkG, magenta), and their overlap
661 (merge). The SSt soma is indicated with an asterisk (*) and the start and end of the
662 AIS localised to that IN indicated (arrows). Scale bar: 10 µm. (**M**) Quantification of the
663 AIS length of SSt INs from WT (N=6 rats, n= 162 AIS) and *16p11.2*$^{+/-}$ (N=6 rats, n=151
664 AIS). (**N**) Quantification of AIS lengths of putative CA1 pyramidal cells from WT (N=6
665 rats, n= 150 AIS) and *16p11.2*$^{+/-}$ (N=6 rats, n=155 AIS) rats. Statistics shown: ns –
666 p>0.05, * - p<0.05, from Linear Mixed Effects modelling.

667

668 To confirm that SSt IN intrinsic excitability changes were not a result of compensation
669 mechanism to altered synaptic input from local CA1 PCs (Booker et al., 2020), we
670 asked whether the spontaneous excitatory postsynaptic currents (EPSC) they receive
671 were different between genotypes. We saw no change in either the spontaneous
672 EPSC amplitude (p=0.4495, LME) or frequency (p=0.2131, LME), implying typical
673 circuit integration of SSt INs to the local network.

674 We confirmed that the effect on intrinsic cell excitability were restricted to SSt INs, by
675 performing recordings from local ExNs – the CA1 PCs. CA1 PCs were identified on

676 the basis of having a somata located in *str. pyramidale,* with a single large-calibre
677 apical dendrite entering *str. radiatum* as observed under IR-DIC. We obtained
678 recordings from 18 putative CA1 PCs per group from 10 WT and 9 *16p11.2*$^{+/-}$ rats. In
679 response to depolarising current injections (0-500 pA, 100 pA steps, Fig. 5H), we
680 observed no change in the number of action potentials generated by the recorded CA1
681 PCs in the *16p11.2*$^{+/-}$ rats compared to WT ($F_{(5, 85)}$=0.9185, P=0.4731, 2-way ANOVA
682 for current/genotype interaction, Fig. 5I). CA1 PCs typically had lower peak action
683 potential discharge rates than for SSt INs (WT: p=3.29x10^{-5}, *16p11.2*$^{+/-}$: p=1.63x10^{-6};
684 LME). Consistent with this lack of altered action potential discharge, we found no
685 change in CA1 PC rheobase current (p=0.7098, LME, Fig. 5J), action potential
686 threshold (p=0.4116, LME, Fig. 5K), or any other parameter tested (Supplementary
687 Table S1). These data strongly suggest that excitatory CA1 PCs are physiologically
688 typical in the *16p11.2* rat model of ASD.

689 We have recently shown that changes to cell excitability effected the voltage threshold
690 and action potential discharge in genetic models of intellectual disability can result
691 from changes to the structure of the axon initial segment (AIS) (Booker et al., 2020).
692 To determine if the changes in SSt IN excitability arise from changes to AIS structure
693 we next performed immunolabelling of perfusion fixed tissue from the hippocampus of
694 WT (N=5) and *16p11.2*$^{+/-}$ (N=5) rats. Immunofluorescent double labelling with
695 AnkyrinG reliably labelled the AIS of all neurons in the CA1 region, which could be
696 identified emerging from the soma, or more often the proximal dendrites of
697 immunolabelled SSt INs (Fig. 5L). Comparison of AIS lengths on SSt INs revealed an
698 11% longer AIS in 16p11.2$^{+/-}$ rats compared to WT (p=0.0064, LME, Fig. 5M). There
699 was no change in the lengths of putative CA1 PC AISs between genotypes (p=0.0962,
700 LME, Fig. 5N).

701 Together, consistent with the hypothesis that the *16p11.2* microdeletion selectively
702 targets INs, these data show a preferential increase of SSt IN excitability in the
703 *16p11.2* rat autism model, with no changes observed in the local excitatory principal
704 cells. This increased cellular excitability coincided with selective alteration to the length
705 of the AIS, corresponding to changes in voltage threshold. Together, these changes
706 could potentially lead to an aberrant network activity and gating of information flow
707 through hippocampal circuits.

708 **DISCUSSION.**

709 This study reveals that molecularly defined classes of INs in the foetal human cerebral
710 cortex display enriched expression of multiple gene transcripts associated with autism.
711 This result is striking, suggesting the testable hypothesis that some INs are
712 disproportionately vulnerable to autism genetic risk factors. Within INs as a whole the
713 most autism associated transcripts are enriched in a subset we described as
714 'IN1,3,5,8' suggesting that these cells may represent a convergent cellular target
715 underpinning genetic predisposition of the developing brain to autism and its co-
716 occuring conditions during post-natal life. This poses the question of what is the
717 identity of these cells? Our data-set was acquired from dissected human foetal cortex,
718 which includes INs that are migrating tangentially through and in the cerebral cortex,
719 but not INs undergoing neurogenesis or early migration in the ganglionic eminences
720 (Hansen et al., 2013; Ma et al., 2013). We examined human foetal cortical cells
721 spanning the interval GW8-26 and found IN1,3,5,8 cells are not present in the cerebral
722 cortex before GW23 and then increase in numbers to GW26. As many INs have
723 migrated into the cortex well before GW23 this suggests that IN1,3,5,8 represent a
724 relatively differentiated stage on the IN developmental trajectory. This is consistent
725 with the enrichment of GO terms relating to synapse maturation and neurite formation
726 in these cells. Transcriptomic similarity between foetal IN1,3,5,8 and adult PV, SST,
727 and VIP INs suggests these cells are destined to form a variety of IN cell types and
728 that changes in their developmental trajectory caused by autism causing mutations
729 may have far reaching consequences for the formation on inhibitory circuitry in the
730 post-natal brain.

731 Although the most striking enrichment of autism associated transcripts was observed
732 in INs we also saw enrichment of some transcripts in other cardinal cell classes.
733 Progenitor cells had a much smaller number of enriched autism associated transcripts
734 than INs and most of these (eg *ADNF*, *ZNF462*, *PHIP*, *HNRNPU*, *RPS6KA3* for
735 monogenic and *PAGR1*, *HIRIP3*, *KIF22*, and *PP4C* for *16p11.2* transcripts). This
736 suggests that progenitor cells in the cerebral cortex may also be vulnerable to a subset
737 of autism causing mutations. Progenitors in the developing neocortex are destined to
738 differentiate into excitatory pyramidal neurons and non-neuronal cell-types (eg
739 astrocytes) suggesting that mutations in these progenitor enriched genes may
740 dysregulate their production or function. This study also prompts future investigation

741 into the expression of autism associated transcripts in IN progenitors located in the
742 ganglionic eminences and the consequence of mutation for IN neurogenesis in
743 humans although our findings in the rat *16p11.2* microdeletion rat model suggest that
744 gross IN output is not affected in this context in rodents.

745 We found that large numbers of monogenic autism risk factor transcripts are highly
746 expressed in IN1,3,5,8 INs, suggesting that their mutation may contribute to the
747 aetiology of autism via alterations to IN development. This hypothesis remains to be
748 tested for the majority of genes. However, for *ARID1B*, *DYRK1A*, *MECP2*, and
749 *CNTNAP2* there is already evidence that monogenic mutation causes abnormal
750 numbers or physiological properties of INs in rodent models (Gao et al., 2018; Jung et
751 al., 2017; Penagarikano et al., 2011; Souchet et al., 2019; Tomassy et al., 2014; Vogt
752 et al., 2018). We also found *KCTD13*, *MAPK3*, and *MVP* transcripts expressed from
753 the *16p11.2* locus are enriched in IN1,3,5,8. *KCTD13* modulates synaptic transmission
754 by suppressing RHOA signalling via interaction with the ubiquitin ligase *CUL3*, itself
755 an autism risk factor (Escamilla et al., 2017; Willsey et al., 2013). *CUL3* is co-
756 expressed with *KCTD13* in IN1,3,5,8 cells suggesting a molecular mechanism for the
757 *16p11.2* microdeletion to impact on cellular and synaptic function via perturbed RHOA
758 signalling. Interestingly, the inhibition of RHOA pathway has been prosposed as a
759 treatment to restore cognition in *16p11.2* mouse models (Martin Lorenzo et al., 2021).
760 *MAPK3* and *MVP* are both implicated in ERK signalling which impacts diverse cellular
761 processes including cell proliferation, migration, and synaptic function. Indeed, a
762 mouse model of *16p11.2* microdeletion shows elevated ERK signalling leading to
763 perturbed cortical development and autism-like phenotypes (Pucilowska et al., 2018;
764 Pucilowska et al., 2015), although the involvement of INs was not tested.

765 Our analysis of the *16p11.2* microdeletion rat indicates that neither ExN or IN number
766 and location were altered in the cerebral cortex or hippocampal region CA1, so it
767 seems unlikely that a numerical excitation/inhibition imbalance is present in the
768 *16p11.2*$^{+/-}$ rat model. However, whole-cell patch-clamp recordings in CA1 revealed
769 intrinsic hyperexcitability of SSt INs, coincident with increases AIS length. No effect
770 was observed in CA1 excitatory neurons. This suggests a mechanism by which the
771 *16p11.2* microdeletion perturbs the E/I balance by selectively altering the intrinsic
772 excitability of INs. Although IN hyperexcitability may lead to greater inhibition within
773 cortical circuits and tilt the E/I balance towards inhibition, the complexity of such

774 circuits interaction makes prediction of the consequences to gross activity difficult.
775 However, SSt INs themselves possess both direct inhibitory and disinhibitory
776 mechanisms within the prototypical CA1 circuit, leading to alterations to synaptic
777 plasticity when measured at the circuit level (Leao et al., 2012). As such, the outcome
778 of greater SSt IN activity may directly lead to altered cognition observed in ASC/ID.
779 Furthermore, a shift in the E/I balance has been identified in the somatosensory cortex
780 of ASC mouse models (including *16p11.2*$^{+/-}$ mice), attributed to homeostatic regulation
781 of IN function (Antoine et al., 2019). Our combined bioinformatic and physiological
782 approach diverges from this view, suggesting that SSt INs in *16p11.2* microdeletion
783 are genetically cued to perturbation from early in their developmental trajectory. A
784 deeper understanding of the functional consequences of SSt hyperexcitability on the
785 E/I balance in cortical circuits and their homeostasis requires further investigation.

786 To conclude, our bioinformatic analysis of developing human foetal cerebral cortex
787 single cell transcriptomes suggests that developing INs are disproportionately
788 vulnerable to genetic autism risk factors, which is supported by physiological
789 correlates in a *16p11.2* microdeletion rat model. This study paves the way for more in
790 depth investigations of how polygenic and monogenic autism risk factors impact on IN
791 development and function.

792

793 **REFERENCES**

794 Antoine, M.W., Langberg, T., Schnepel, P., Feldman, D.E., 2019. Increased
795 Excitation-Inhibition Ratio Stabilizes Synapse and Circuit Excitability in Four Autism
796 Mouse Models. Neuron 101, 648-661 e644.
797 Blumenthal, I., Ragavendran, A., Erdin, S., Klei, L., Sugathan, A., Guide, J.R.,
798 Manavalan, P., Zhou, J.Q., Wheeler, V.C., Levin, J.Z., Ernst, C., Roeder, K., Devlin,
799 B., Gusella, J.F., Talkowski, M.E., 2014. Transcriptional consequences of 16p11.2
800 deletion and duplication in mouse cortex and multiplex autism families. Am J Hum
801 Genet 94, 870-883.
802 Booker, S.A., Simoes de Oliveira, L., Anstey, N.J., Kozic, Z., Dando, O.R., Jackson,
803 A.D., Baxter, P.S., Isom, L.L., Sherman, D.L., Hardingham, G.E., Brophy, P.J.,
804 Wyllie, D.J.A., Kind, P.C., 2020. Input-Output Relationship of CA1 Pyramidal

805 Neurons Reveals Intact Homeostatic Mechanisms in a Mouse Model of Fragile X
806 Syndrome. Cell Rep 32, 107988.
807 Booker, S.A., Vida, I., 2018. Morphological diversity and connectivity of hippocampal
808 interneurons. Cell Tissue Res 373, 619-641.
809 Bozzi, Y., Provenzano, G., Casarosa, S., 2018. Neurobiological bases of autism-
810 epilepsy comorbidity: a focus on excitation/inhibition imbalance. Eur J Neurosci 47,
811 534-548.
812 Crow, M., Paul, A., Ballouz, S., Huang, Z.J., Gillis, J., 2018. Characterizing the
813 replicability of cell types defined by single cell RNA-sequencing data using
814 MetaNeighbor. Nat Commun 9, 884.
815 Escamilla, C.O., Filonova, I., Walker, A.K., Xuan, Z.X., Holehonnur, R., Espinosa, F.,
816 Liu, S., Thyme, S.B., Lopez-Garcia, I.A., Mendoza, D.B., Usui, N., Ellegood, J.,
817 Eisch, A.J., Konopka, G., Lerch, J.P., Schier, A.F., Speed, H.E., Powell, C.M., 2017.
818 Kctd13 deletion reduces synaptic transmission via increased RhoA. Nature 551, 227-
819 231.
820 Gao, R., Piguel, N.H., Melendez-Zaidi, A.E., Martin-de-Saavedra, M.D., Yoon, S.,
821 Forrest, M.P., Myczek, K., Zhang, G., Russell, T.A., Csernansky, J.G., Surmeier,
822 D.J., Penzes, P., 2018. CNTNAP2 stabilizes interneuron dendritic arbors through
823 CASK. Mol Psychiatry 23, 1832-1850.
824 Hansen, D.V., Lui, J.H., Flandin, P., Yoshikawa, K., Rubenstein, J.L., Alvarez-Buylla,
825 A., Kriegstein, A.R., 2013. Non-epithelial stem cells and cortical interneuron
826 production in the human ganglionic eminences. Nat Neurosci 16, 1576-1587.
827 Horev, G., Ellegood, J., Lerch, J.P., Son, Y.E., Muthuswamy, L., Vogel, H., Krieger,
828 A.M., Buja, A., Henkelman, R.M., Wigler, M., Mills, A.A., 2011. Dosage-dependent
829 phenotypes in models of 16p11.2 lesions found in autism. Proc Natl Acad Sci U S A
830 108, 17076-17081.
831 Jung, E.M., Moffat, J.J., Liu, J., Dravid, S.M., Gurumurthy, C.B., Kim, W.Y., 2017.
832 Arid1b haploinsufficiency disrupts cortical interneuron development and mouse
833 behavior. Nat Neurosci 20, 1694-1707.
834 Lake, B.B., Chen, S., Sos, B.C., Fan, J., Kaeser, G.E., Yung, Y.C., Duong, T.E.,
835 Gao, D., Chun, J., Kharchenko, P.V., Zhang, K., 2018. Integrative single-cell analysis
836 of transcriptional and epigenetic states in the human adult brain. Nat Biotechnol 36,
837 70-80.

838 Leao, R.N., Mikulovic, S., Leao, K.E., Munguba, H., Gezelius, H., Enjin, A., Patra, K.,
839 Eriksson, A., Loew, L.M., Tort, A.B., Kullander, K., 2012. OLM interneurons
840 differentially modulate CA3 and entorhinal inputs to hippocampal CA1 neurons. Nat
841 Neurosci 15, 1524-1530.
842 Ma, T., Wang, C., Wang, L., Zhou, X., Tian, M., Zhang, Q., Zhang, Y., Li, J., Liu, Z.,
843 Cai, Y., Liu, F., You, Y., Chen, C., Campbell, K., Song, H., Ma, L., Rubenstein, J.L.,
844 Yang, Z., 2013. Subcortical origins of human and monkey neocortical interneurons.
845 Nat Neurosci 16, 1588-1597.
846 Martin Lorenzo, S., Nalesso, V., Chevalier, C., Birling, M.C., Herault, Y., 2021.
847 Targeting the RHOA pathway improves learning and memory in adult Kctd13 and
848 16p11.2 deletion mouse models. Mol Autism 12, 1.
849 Mayer, C., Hafemeister, C., Bandler, R.C., Machold, R., Batista Brito, R., Jaglin, X.,
850 Allaway, K., Butler, A., Fishell, G., Satija, R., 2018. Developmental diversification of
851 cortical inhibitory interneurons. Nature 555, 457-462.
852 Morson, S., Yang, Y., Price, D.J., Pratt, T., 2021. Expression of Genes in the
853 16p11.2 Locus during Development of the Human Fetal Cerebral Cortex. Cereb
854 Cortex.
855 Nelson, S.B., Valakh, V., 2015. Excitatory/Inhibitory Balance and Circuit
856 Homeostasis in Autism Spectrum Disorders. Neuron 87, 684-698.
857 Oliveira, L.S., Sumera, A., Booker, S.A., 2021. Repeated whole-cell patch-clamp
858 recording from CA1 pyramidal cells in rodent hippocampal slices followed by axon
859 initial segment labeling. STAR Protoc 2, 100336.
860 Packer, A., 2016. Neocortical neurogenesis and the etiology of autism spectrum
861 disorder. Neurosci Biobehav Rev 64, 185-195.
862 Penagarikano, O., Abrahams, B.S., Herman, E.I., Winden, K.D., Gdalyahu, A., Dong,
863 H., Sonnenblick, L.I., Gruver, R., Almajano, J., Bragin, A., Golshani, P.,
864 Trachtenberg, J.T., Peles, E., Geschwind, D.H., 2011. Absence of CNTNAP2 leads
865 to epilepsy, neuronal migration abnormalities, and core autism-related deficits. Cell
866 147, 235-246.
867 Pucilowska, J., Vithayathil, J., Pagani, M., Kelly, C., Karlo, J.C., Robol, C., Morella,
868 I., Gozzi, A., Brambilla, R., Landreth, G.E., 2018. Pharmacological Inhibition of ERK
869 Signaling Rescues Pathophysiology and Behavioral Phenotype Associated with
870 16p11.2 Chromosomal Deletion in Mice. J Neurosci 38, 6640-6652.

871 Pucilowska, J., Vithayathil, J., Tavares, E.J., Kelly, C., Karlo, J.C., Landreth, G.E.,
872 2015. The 16p11.2 deletion mouse model of autism exhibits altered cortical
873 progenitor proliferation and brain cytoarchitecture linked to the ERK MAPK pathway.
874 J Neurosci 35, 3190-3200.
875 Puts, N.A.J., Wodka, E.L., Harris, A.D., Crocetti, D., Tommerdahl, M., Mostofsky,
876 S.H., Edden, R.A.E., 2017. Reduced GABA and altered somatosensory function in
877 children with autism spectrum disorder. Autism Res 10, 608-619.
878 Qiu, Y., Arbogast, T., Lorenzo, S.M., Li, H., Tang, S.C., Richardson, E., Hong, O.,
879 Cho, S., Shanta, O., Pang, T., Corsello, C., Deutsch, C.K., Chevalier, C., Davis,
880 E.E., Iakoucheva, L.M., Herault, Y., Katsanis, N., Messer, K., Sebat, J., 2019.
881 Oligogenic Effects of 16p11.2 Copy-Number Variation on Craniofacial Development.
882 Cell Rep 28, 3320-3328 e3324.
883 Rapanelli, M., Frick, L.R., Pittenger, C., 2017. The Role of Interneurons in Autism
884 and Tourette Syndrome. Trends Neurosci 40, 397-407.
885 Robertson, C.E., Ratai, E.M., Kanwisher, N., 2016. Reduced GABAergic Action in
886 the Autistic Brain. Curr Biol 26, 80-85.
887 Souchet, B., Duchon, A., Gu, Y., Dairou, J., Chevalier, C., Daubigney, F., Nalesso,
888 V., Creau, N., Yu, Y., Janel, N., Herault, Y., Delabar, J.M., 2019. Prenatal treatment
889 with EGCG enriched green tea extract rescues GAD67 related developmental and
890 cognitive defects in Down syndrome mouse models. Sci Rep 9, 3914.
891 Tai, D.J., Ragavendran, A., Manavalan, P., Stortchevoi, A., Seabra, C.M., Erdin, S.,
892 Collins, R.L., Blumenthal, I., Chen, X., Shen, Y., Sahin, M., Zhang, C., Lee, C.,
893 Gusella, J.F., Talkowski, M.E., 2016. Engineering microdeletions and
894 microduplications by targeting segmental duplications with CRISPR. Nat Neurosci
895 19, 517-522.
896 Tomassy, G.S., Morello, N., Calcagno, E., Giustetto, M., 2014. Developmental
897 abnormalities of cortical interneurons precede symptoms onset in a mouse model of
898 Rett syndrome. J Neurochem 131, 115-127.
899 Vogt, D., Cho, K.K.A., Shelton, S.M., Paul, A., Huang, Z.J., Sohal, V.S., Rubenstein,
900 J.L.R., 2018. Mouse Cntnap2 and Human CNTNAP2 ASD Alleles Cell Autonomously
901 Regulate PV+ Cortical Interneurons. Cereb Cortex 28, 3868-3879.
902 Willsey, A.J., Sanders, S.J., Li, M., Dong, S., Tebbenkamp, A.T., Muhle, R.A., Reilly,
903 S.K., Lin, L., Fertuzinhos, S., Miller, J.A., Murtha, M.T., Bichsel, C., Niu, W., Cotney,
904 J., Ercan-Sencicek, A.G., Gockley, J., Gupta, A.R., Han, W., He, X., Hoffman, E.J.,

905 Klei, L., Lei, J., Liu, W., Liu, L., Lu, C., Xu, X., Zhu, Y., Mane, S.M., Lein, E.S., Wei,
906 L., Noonan, J.P., Roeder, K., Devlin, B., Sestan, N., State, M.W., 2013.
907 Coexpression networks implicate human midfetal deep cortical projection neurons in
908 the pathogenesis of autism. Cell 155, 997-1007.
909 Zhong, S., Zhang, S., Fan, X., Wu, Q., Yan, L., Dong, J., Zhang, H., Li, L., Sun, L.,
910 Pan, N., Xu, X., Tang, F., Zhang, J., Qiao, J., Wang, X., 2018. A single-cell RNA-seq
911 survey of the developmental landscape of the human prefrontal cortex. Nature 555,
912 524-528.

913

914

915

916

917

918

919

920

921

922

923

924

925

926

927

928

929

930

931 **SUPPLEMENTARY FIGURES**

Figure S1

A

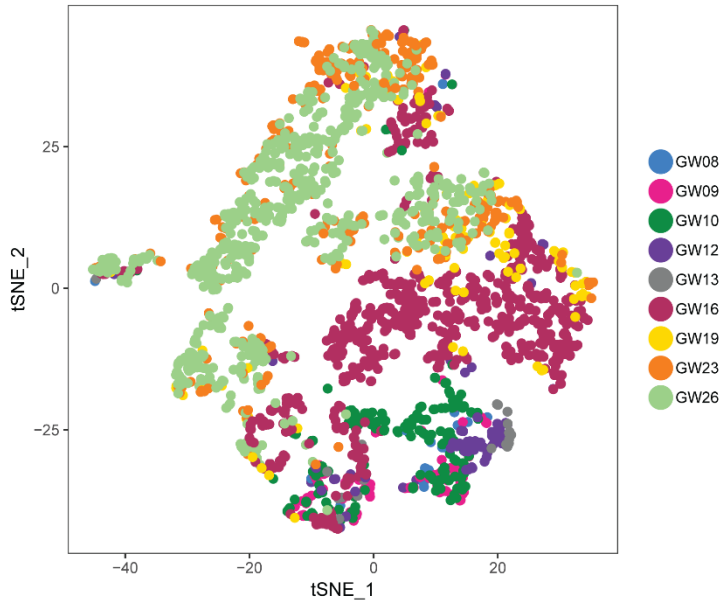

B

Cell class	PCW	# of cells	Cell class	PCW	# of cells	Cell class	PCW	# of cells
	GW08	3		GW08	15		GW08	3
	GW09	50		GW09	35		GW09	3
	GW10	83		GW10	93		GW10	7
	GW12	12		GW12	63		GW12	7
NPCs	GW13	7	**ExNs**	GW13	16	**INs**	GW13	0
	GW16	123		GW16	545		GW16	83
	GW19	5		GW19	82		GW19	22
	GW23	2		GW23	89		GW23	174
	GW26	4		GW26	118		GW26	402
	Total	**289**		**Total**	**1056**		**Total**	**701**
Cell class	PCW	# of cells	Cell class	PCW	# of cells	Cell class	PCW	# of cells
	GW08	0		GW08	0		GW08	2
	GW09	0		GW09	0		GW09	0
	GW10	0		GW10	0		GW10	1
	GW12	2		GW12	0		GW12	1
OPCs	GW13	0	**AST**	GW13	0	**MIC**	GW13	1
	GW16	14		GW16	0		GW16	11
	GW19	4		GW19	6		GW19	1
	GW23	25		GW23	7		GW23	10
	GW26	72		GW26	63		GW26	40
	Total	**117**		**Total**	**76**		**Total**	**67**

B

932

933 **Figure S1 (A)** *t*-SNE plot showing the distribution of foetal stages **(B)** table showing
934 numbers of cells of each cardinal class at each foetal stage.

935

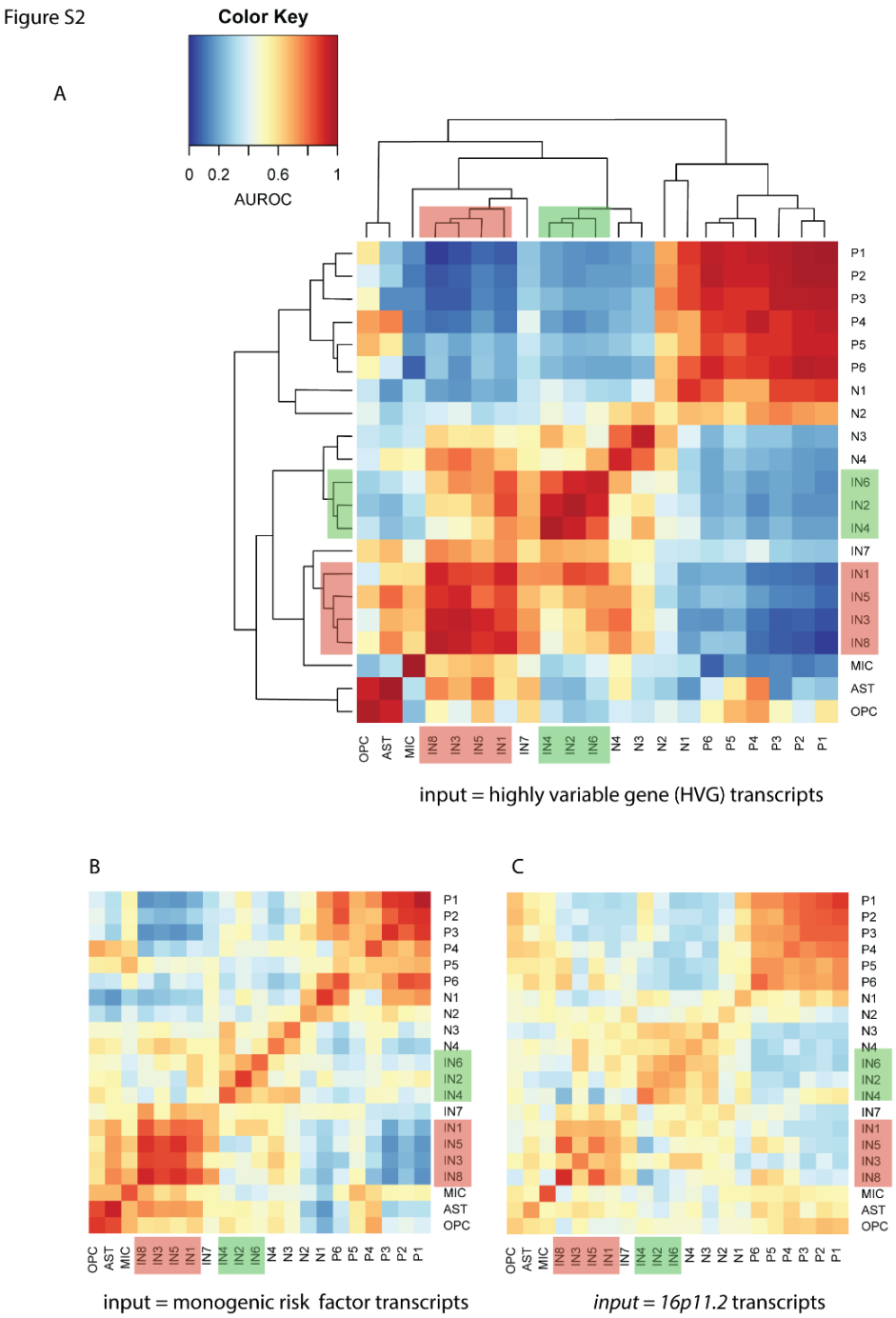

Figure S2 Pairwise comparison of the cluster similarity calculated by MetaNeighbor between the 21 cell clusters. AUROC scores represented as a heatmap where high similarity between clusters is coloured red and low similarity blue. Three plots are shown using different input gene sets **(A)** ~2000 highly variable gene transcripts between clusters. **(B)** the 83 high confidence and strong candidate (SFARI lists 1 and 2) monogenic autism risk factor transcripts. **(C)** the 27 *16p11.2* transcripts.

Figure S3

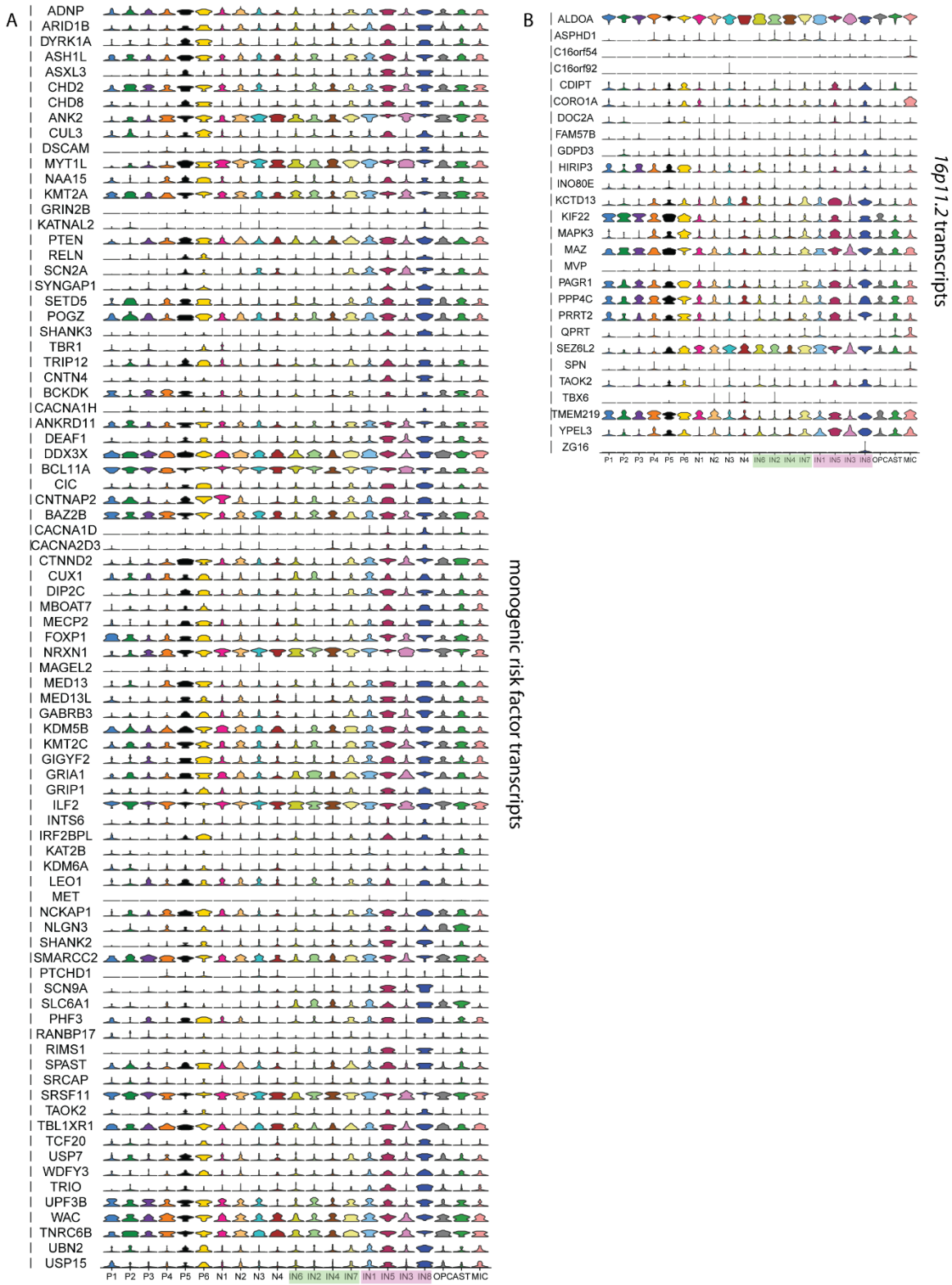

Figure S3 Violin plots showing transcript levels in the 21 different clusters for **(A)** the 83 high confidence and strong candidate (SFARI lists 1 and 2) monogenic autism risk transcripts and **(B)** the 27 *16p11.2* transcripts.

947

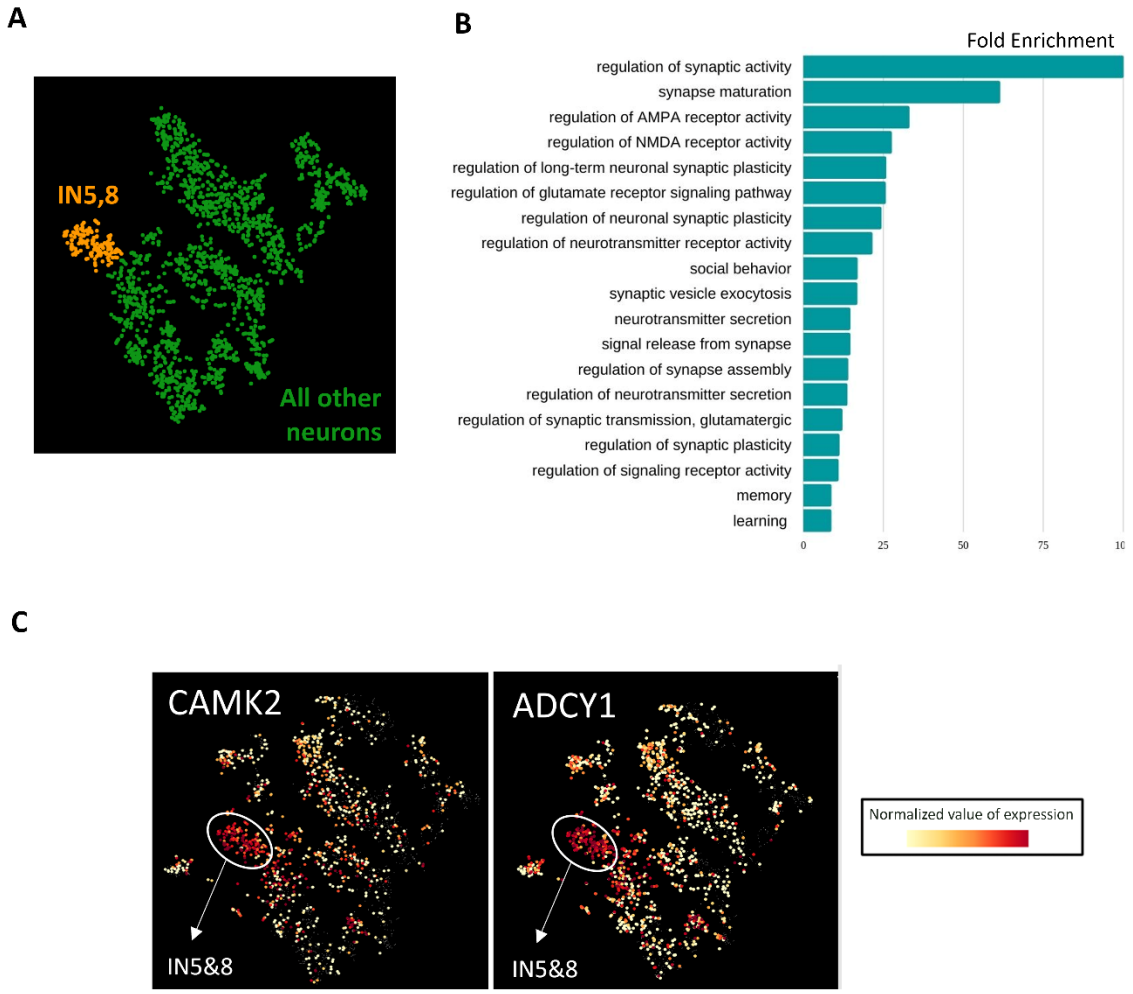

948

949 **Figure S4**. Characterisation of INs by gene ontology analysis. Gene ontology (GO)
950 analysis in IN5,8 (orange in A) versus all other cells (green in A) reveals enrichment
951 of GO terms associated with (B) synaptic activity, maturation, and plasticity. (C)
952 gradient plots of CAMK2, ADCY1 showing that these transcripts are most highly
953 expressed in IN5,8.

954

955

956

957

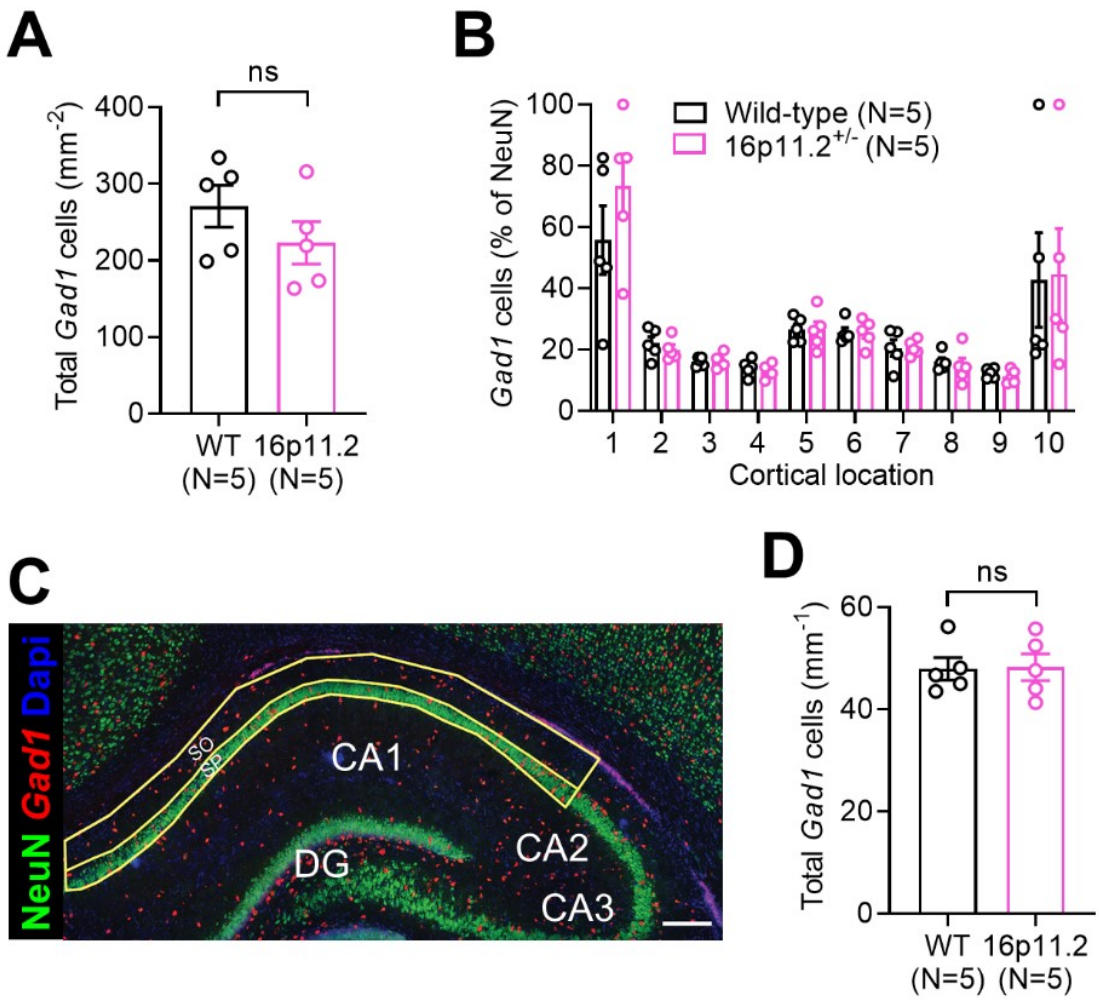

Figure S5: No change in total IN number in somatosensory cortex or hippocampus of the *16p11.2*$^{+/-}$ rat. (A) Based on the expression of *Gad1* mRNA, quantification of the total number of INs across the whole somatosensory column from WT (N=6) and *16p11.2*$^{+/-}$ (N=6) rats. (**B**) No change in the relative ratio of *Gad1*-positive cells to total neurons (NeuN) was observed within the cortical column. (**C**) Expanded view of CA1 of the hippocampus from the same image as in Figure 5A, showing Gad1 in situ hybridisation (red), NeuN immunolabelling (green) and DAPI nuclei (blue). Regions used for cell counts in *str. pyramidale* (SP) and *str. oriens* (SO) are delineated with yellow lines. Scale bar: 200 µm. (**D**) Total number of *Gad1*-positive neurons measured in CA1 from WT (N=5) and *16p11.2*$^{+/-}$ (N=5) rats. Statistics shown: ns – p>0.05 from Student's 2-tailed t-test.

972 **SUPPLEMENTARY TABLES**

973 **Table S1**

974

	SSt INs			CA1 pyramidal cells		
Parameter tested	Wild-type	16p11.2$^{+/-}$	*p*	Wild-type	16p11.2$^{+/-}$	*p*
n (N)	30 (15)	18 (13)		18 (10)	18(9)	
Resting membrane potential (mV)	-56.6 ± 1.5	-60.9 ± 1.8	0.25	-64.6 ± 1.9	-65.3 ± 1.1	0.88
Input resistance (MΩ)	204 ± 22	220 ± 26	0.65	113 ± 15	105 ± 18	0.73
Membrane time-constant (ms)	34.5 ± 5.3	34.9 ± 6.3	0.72	24.2 ± 1.7	23.0 ± 2.3	0.74
Membrane capacitance (pF)	162 ± 11	152 ± 16	0.30	239 ± 17	245 ± 16	0.97
Voltage sag (mV)	18.2 ± 1.7	17.9 ± 2.0	0.50	8.4 ± 0.6	9.4 ± 1.2	0.43
Sag (% of maximum)	32.9 ± 2.2	36.0 ± 3.7	0.76	23.9 ± 1.6	25.1 ± 1.5	0.65
Rheobase (pA)	233 ± 22	194 ± 28	0.11	256 ± 28	266 ± 20	0.71
Voltage threshold (mV)	-39.6 ± 0.7	-42.1 ± 0.9	**0.03**	-42.4 ± 1.3	-41.9 ± 1.0	0.41
AP amplitude (mV)	98.3 ± 3.2	97.7 ± 3.3	0.64	122.5 ± 1.8	119.8 ± 2.9	0.61
AP 20-80% rise-time (ms)	0.17 ± 0.01	0.16 ± 0.01	0.38	0.15 ± 0.01	0.16 ± 0.01	0.87
AP half-height duration (ms)	0.62 ± 0.02	0.61 ± 0.04	0.81	1.00 ± 0.02	0.98 ± 0.03	0.60
AP max. rise-rate (mV.ms^{-1})	276 ± 18	310 ± 22	0.48	455 ± 19	443 ± 29	0.96
AP max. decay-rate (mV.ms^{-1})	124 ± 7	139 ± 13	0.53	77 ± 1	79 ± 4	0.64
Peak firing (Hz)	54.8 ± 5.0	71.6 ± 7.9	**0.02**	30.3 ± 3.1	31.4 ± 1.8	0.70

975

976

977

978

979